Nanoscale

REVIEW

View Article Online
View Journal

Cite this: DOI: 10.1039/d5nr05470b

Advanced gas sensors *via* nanoscale structure engineering and fabrication strategies

Ju-Ah Jin,†[a] Seong-Jin Park,†[a] Ho-Jae Kim,†[b] Geumbee Lee,*[c] Sang Min Won *[b] and Jae-Young Yoo *[a,b]

Recent progress in nanoscale materials engineering has reshaped the field of gas sensing, transforming it from empirical material substitution into a design discipline that links fabrication, structure, and performance. This review provides a comprehensive overview of fabrication strategies for nanostructured gas sensors, categorized into three main fabrication processes: wet, dry and hybrid dry–wet fabrication approaches. Wet-synthesis techniques including hydrothermal growth, sol–gel processing, and electrospinning enable the formation of nanowires, nanosheets, and porous networks with a high surface area, controlled morphology, and rich defect chemistry that enhance gas adsorption and charge transfer. Dry-fabrication methods such as physical vapor deposition, plasma etching, and atomic layer deposition provide precise dimensional control, wafer-scale reproducibility, and excellent compatibility with integrated electronic platforms, facilitating scalable and uniform device construction. Hybrid dry–wet fabrication strategies integrate the structural versatility of wet chemistry with the deterministic precision of dry processing to produce hierarchical and conformal nanostructures that optimize gas–solid interactions and enable high-performance device integration. Through a comparative analysis of the recent literature, this review correlates fabrication parameters with the resulting nanostructural features such as porosity, crystallinity, and junction density, and discusses their influence on sensing metrics including sensitivity, selectivity, response and recovery dynamics, and long-term stability. Emerging trends in low-power operation, reproducible array fabrication, and integration with flexible and CMOS-compatible substrates are also highlighted, reflecting the ongoing transition of gas sensors toward intelligent, networked, and application-ready systems. By establishing a process-aware framework that links fabrication design with functional performance, this review aims to guide the rational development of next-generation nanostructured gas sensors for environmental, industrial, and healthcare applications.

Received 28th December 2025,
Accepted 1st April 2026

DOI: 10.1039/d5nr05470b

rsc.li/nanoscale

1. Introduction

In recent years, the detection and monitoring of hazardous and trace gases have become increasingly important for environmental protection, industrial safety, healthcare diagnostics, and smart-city development. Toxic gases such as NO_2, CO, and H_2S, and volatile organic compounds (VOCs) contribute to air pollution, workplace hazards, and disease progression, while flammable gases like H_2 and CH_4 pose risks of explosion and fire. Consequently, the demand for highly sensitive, selective, and energy-efficient gas sensors capable of real-time monitoring under ambient conditions has grown dramatically.[1–4] Gas-sensing technologies are now recognized as essential components in Internet of Things (IoT) networks, wearable electronics, and distributed environmental monitoring platforms, enabling early detection, safety automation, and personalized healthcare.[3,4]

Traditional detection methods, such as optical spectroscopy, gas chromatography, and electrochemical sensing, offer high precision but suffer from high cost, bulky instrumentation, and limited portability. In contrast, semiconducting solid-state gas sensors, particularly those based on metal oxides and two-dimensional materials, offer miniaturization, fast response, and low-cost integration, making them ideal for scalable, continuous sensing applications.[1,2,5–7] Among diverse sensing platforms, metal oxide semiconductors (MOSs), two-dimensional (2D) materials, and carbon-based materials have been most extensively investigated. MOSs are the most established option because their chemiresistive response is governed by well-defined surface oxygen chemistry

[a]Department of Semiconductor Convergence Engineering, Sungkyunkwan University, Republic of Korea. E-mail: jy.yoo@skku.edu
[b]Department of Electrical and Computer Engineering, Sungkyunkwan University, Republic of Korea. E-mail: sangminwon@skku.edu
[c]School of Chemical Engineering and Applied Chemistry, Kyungpook National University, Republic of Korea. E-mail: geumbee.lee@knu.ac.kr
†These authors contributed equally to this work.

and depletion-layer modulation, while their robustness and process compatibility support scalable and reproducible device manufacturing.[8,9] Two-dimensional materials offer surface-dominated transport in an ultrathin channel, where adsorption-induced charge transfer can efficiently modulate conductance at reduced operating temperatures and, in some cases, at room temperature; moreover, distinct basal-plane *versus* edge/defect sites can be leveraged to improve selectivity through morphology control and heterostructure engineering.[10,11] Carbon-based materials such as graphene and reduced graphene oxide typically function as highly conductive networks and signal amplifiers in hybrid sensors, facilitating interfacial charge transfer and mechanically compliant architectures for flexible and wearable platforms. However, these conventional thin-film or bulk devices often exhibit limited active surface area, slow response/recovery, and poor long-term stability, especially at room temperature or under variable humidity. Overcoming these challenges requires rethinking materials and architectures at the nanoscale.[19]

To address these limitations, nanostructured materials have emerged as a transformative platform for gas-sensing technologies. Their inherently large surface-to-volume ratio, high density of active sites, and tunable charge-transport pathways dramatically enhance gas adsorption and charge-transfer processes,[1,6,7] leading to faster kinetics, lower detection limits, and improved operational stability.[20–22] These attributes establish nanoscale engineering as a fundamental strategy for achieving high-performance gas sensors suitable for next-generation applications.

Recent advances in nanoengineering demonstrate that gas-sensor performance depends not only on the chemical composition of materials but also on the geometric configuration, dimensionality, and interfacial architecture controlled during fabrication.[1,23] For instance, one-dimensional (1D) nanowires and fibrous networks facilitate directional charge transport and efficient gas diffusion,[13,24–26] while two- and three-dimensional (2D/3D) porous frameworks maximize surface accessibility and catalytic reactivity.[27–29] Such structural control bridges material synthesis and device integration, enabling tunable sensitivity and robustness under diverse operating conditions.[30–32]

To fully exploit these advantages, fabrication strategies have evolved from conventional thin-film deposition to advanced nanoscale fabrication routes, which can be broadly categorized into dry, wet, and hybrid processes (Fig. 1). Dry micro/nanofabrication, such as etching and deposition processes, provides deterministic patterning and seamless integration with MEMS or CMOS circuitry, offering wafer-scale reproducibility and compact architectures ideal for on-chip systems.[12,13,30] Conversely, wet-chemical methods, such as hydrothermal synthesis, sol–gel processing, and electrospinning, enable cost-effective and large-area growth of nanostructures with tunable porosity and surface functionality.[14,15,25,26,28,29] More recently, hybrid dry–wet fabrication schemes combining top-down patterning with *in situ* chemical growth have emerged, merging structural precision with morphological versatility to produce hierarchical architectures with strong adhesion and high reactivity.[18]

This review aims to provide a sensing performance and industrialization perspective on nanoengineered gas sensors, systematically linking the fabrication strategy, nanoscale architecture, and device performance. By establishing quantitative and qualitative correlations across different fabrication routes, we offer a practical framework for selecting fabrication strategies that align with the desired morphology, integration level, and sensing objectives. Through this lens, we highlight how rational nanoengineering can enable the design of high-performance, scalable, and energy-efficient gas sensors for emerging applications in environmental, industrial, and healthcare monitoring.

Jae-Young Yoo

Prof. Jae-Young Yoo is an associate professor in the Department of Semiconductor Convergence Engineering at Sungkyunkwan University. He received his B.S., M.S., and Ph.D. in Electrical Engineering from KAIST. He previously worked as a postdoctoral researcher at Northwestern University's Querrey Simpson Institute for Bioelectronics. His research focuses on highly reliable medical sensors, wireless systems, and real-time analysis of vital signals. He has published numerous papers in leading journals, including Science, Nature, Nature Medicine, Nature Electronics, and Advanced Materials, contributing to advancements in bioelectronics and nanostructured sensor technologies.

2. Advantages of nanostructured gas sensors

The gas-sensing behavior of metal–oxide semiconductors (MOS) originates from the coupling between surface redox reactions and the modulation of electronic transport within the sensing layer. When exposed to ambient air, oxygen molecules are chemisorbed on the oxide surface, extracting electrons from n-type or trapping holes from p-type semiconductors to form negatively charged species such as O_2^-, O^-, and O^{2-}. This charge transfer leads to the formation of an interfacial space-charge region—known as the electron depletion layer (EDL) in n-type semiconductors and the hole accumulation layer (HAL) in p-type materials—which defines the baseline resistance of the sensing layer (Fig. 2a).

The sensing process proceeds through two major stages: first, the establishment of equilibrium between surface oxygen ions and charge carriers in air, and second, the modulation of

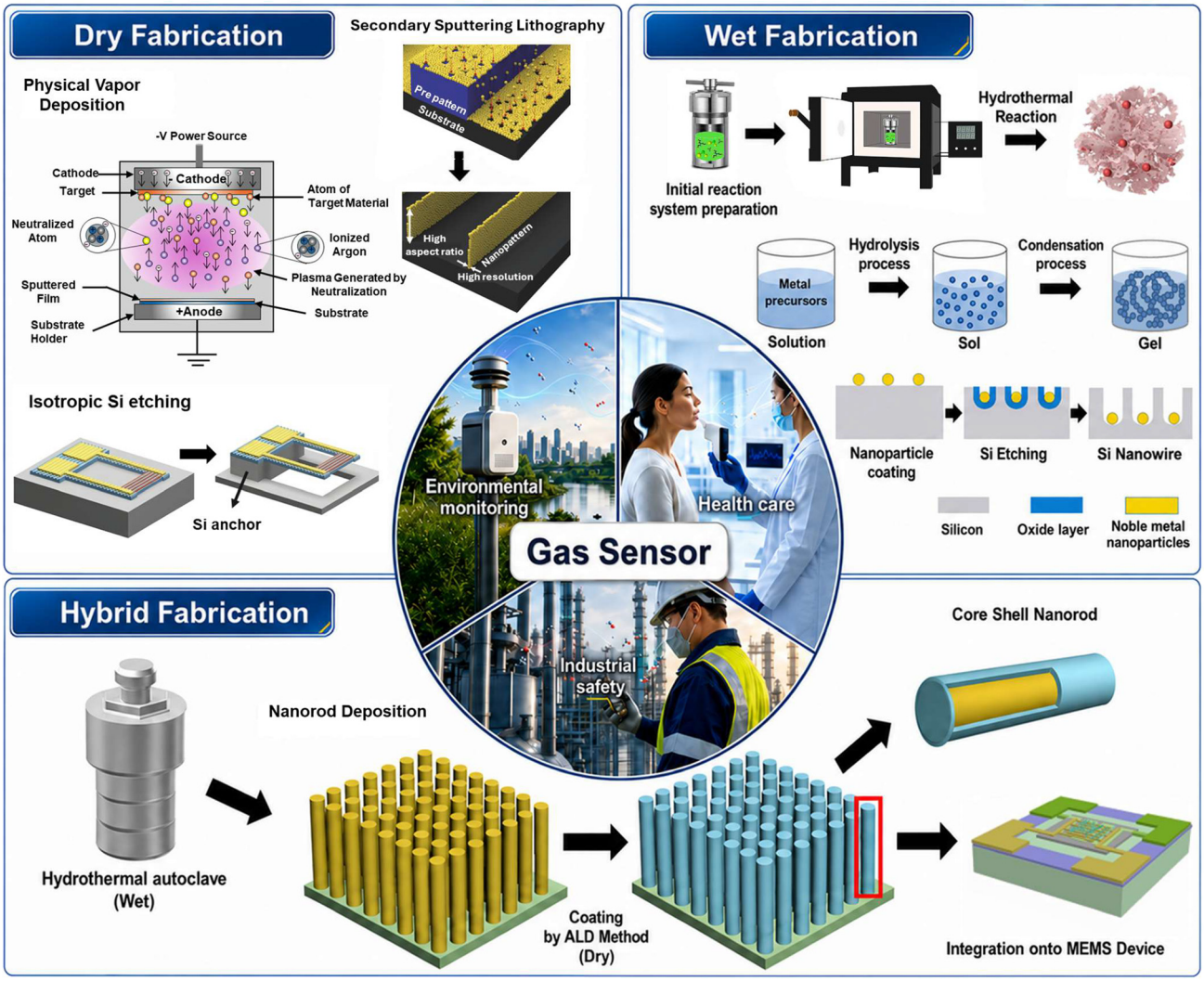

Fig. 1 Schematic illustrations of advanced nanostructure fabrication strategies for gas-sensing applications, categorized into dry-fabrication, wet-fabrication, and hybrid dry–wet fabrication approaches, together with representative application fields. Dry-fabrication routes include PVD sputtering, secondary sputtering lithography for high-aspect-ratio nanopatterns, and isotropic Si etching to form air-suspended nanowire heater arrays. Adapted with permission from refs. 12 and 13 Copyright 2014–2020, Wiley-VCH GmbH. Wet-fabrication routes comprise hydrothermal synthesis, sol–gel processing, and metal-assisted chemical etching (MACE), which are used to form gas-sensing nanostructures. Adapted from refs. 14–17 Licensed under CC BY 4.0. The hybrid dry–wet strategy integrates top-down microheater patterning with bottom-up hydrothermal growth of hierarchical oxide nanostructures on MEMS platforms. Adapted with permission from ref. 18 Copyright 2022, Elsevier.

this equilibrium upon exposure to a target gas. When a reducing gas (*e.g.*, CO, H_2, and NH_3) interacts with the surface, it reacts with pre-adsorbed oxygen species, releasing trapped electrons back into the semiconductor lattice. This reaction reduces band bending, narrows the depletion layer, and decreases resistance in n-type materials. Conversely, for p-type oxides such as CuO, NiO, or Co_3O_4, the released electrons recombine with holes, suppressing the HAL and increasing resistance. Oxidizing gases (*e.g.*, NO_2 and O_3) have the opposite effect, withdrawing electrons from the conduction band or trapping them *via* surface reactions, thereby widening the depletion layer and increasing resistance in n-type semiconductors while decreasing resistance in p-type materials.[33,34]

The reactivity of chemisorbed oxygen species is strongly dependent on temperature. At low temperatures (below ~150 °C), adsorbed oxygen mainly exists as O_2^-, whereas between 200 and 400 °C, atomic species such as O^- and O^{2-} become dominant. This thermal activation behavior explains the enhanced response and recovery observed at intermediate temperatures, where surface reactions are kinetically favorable but not diffusion limited. Oxygen vacancies also play a critical role by acting as donor sites for oxygen adsorption and influencing carrier concentration. Meanwhile, morphological parameters—including grain size, porosity, and inter-grain connectivity—govern the spatial extent of depletion and charge transport across the sensing film.[35]

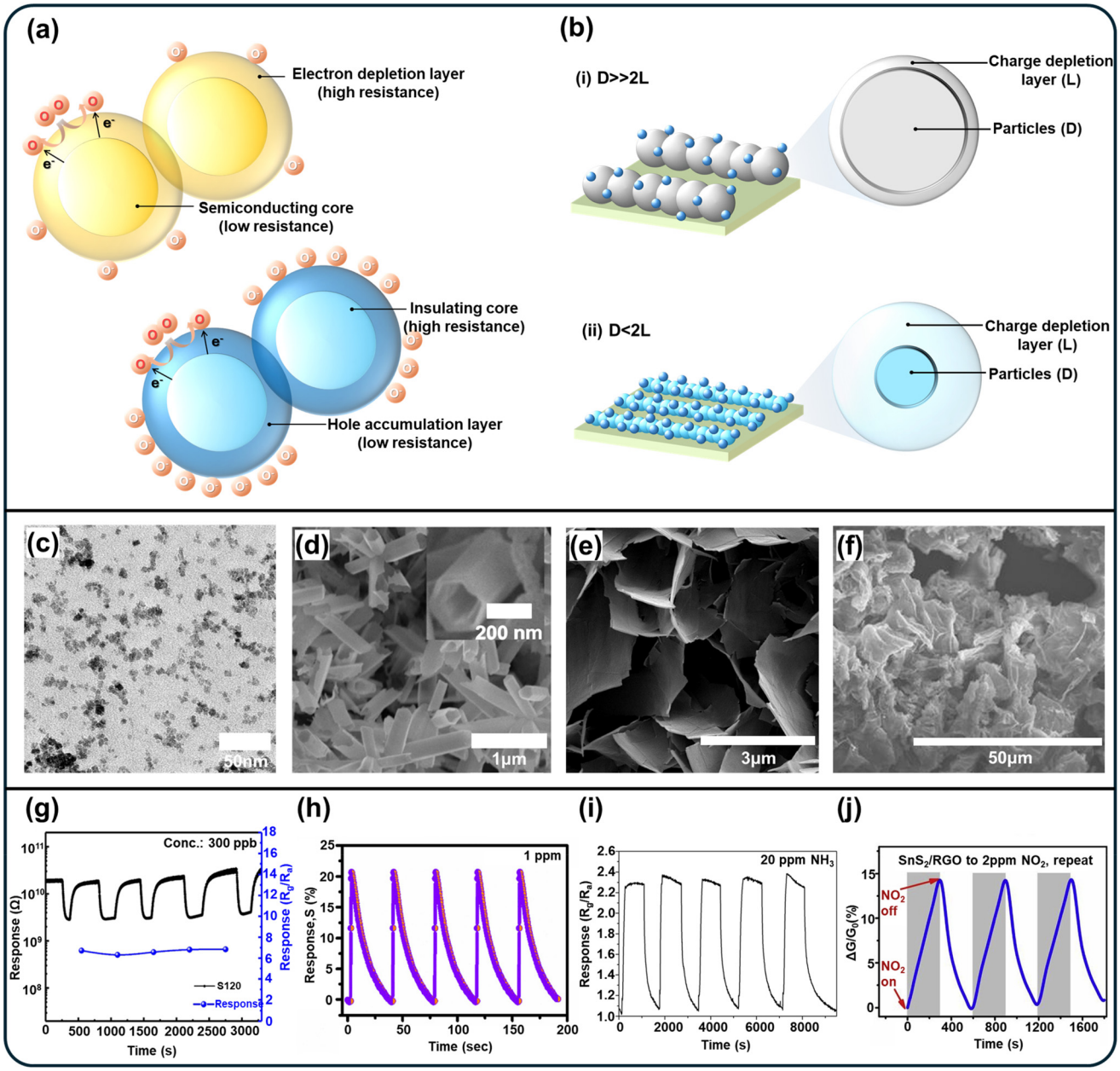

Fig. 2 Schematic illustration of the advantages of nanostructuring in gas-sensing materials. (a) Schematic sensing mechanisms of n-type and p-type semiconductors induced by oxygen chemisorption. Adapted with permission from ref. 33 Copyright 2014, Elsevier. (b) Crystallite-size-dependent depletion behavior ($D \gg 2L$ *vs.* $D < 2L$; with D the particle (crystallite) diameter and L the charge depletion layer thickness). Adapted with permission from ref. 35 Copyright 2004, AIP Publishing. (c and g) Scanning electron microscopy (SEM) image and gas-response characteristics of a 0D TiO_2 quantum-dot sensor. Adapted with permission from ref. 37 Copyright 2022, Elsevier. (d and h) SEM image and gas-response characteristics of 1D ZnO nanotubes. Adapted from ref. 38 Licensed under CC BY 4.0. (e and i) SEM image and gas-response characteristics of 2D Co_3O_4 nanosheet networks. Adapted with permission from ref. 39 Copyright 2016, Elsevier. (f and j) SEM image and gas-response characteristics of 3D SnS_2/rGO heterostructures. Adapted with permission from ref. 40 Copyright 2020, Elsevier.

Consequently, the sensing performance of MOS devices is determined not only by their intrinsic chemistry but also by how structural and morphological design modulates charge-transfer dynamics. To describe this relationship quantitatively, the response of semiconducting oxides can be modeled by incorporating grain size (D_G), inter-grain contact (D_C), and surface potential variation ($\Delta\Phi$) into a transport-based framework.[35,36] The response ratio between air and gas atmospheres is expressed as follows:

$$S = \frac{R_{air}}{R_{gas}} = \frac{\frac{D_C}{L_D}\exp\left(-\frac{qV_{Air}}{2kT}\right) + 1 + \frac{D_G}{L_D}\exp\left(-\frac{qV_{Air}}{2kT}\right)}{\frac{D_C}{L_D}\exp\left[-\frac{q(V_{Air}+\Delta\Phi)}{2kT}\right] + 1 + \frac{D_G}{L_D}\exp\left[-\frac{q(V_{Air}+\Delta\Phi)}{2kT}\right]}$$

where L_D is the Debye length, V_{Air} represents the surface potential in air, and $\Delta\Phi$ corresponds to the potential change induced by gas adsorption. This analytical expression highlights that the sensing signal exhibits exponential dependence on both electronic ($\Delta\Phi$) and morphological (D_G, D_C, and L_D) parameters. As the characteristic grain size and contact dimension approach the Debye length ($L_D \approx D_G$, D_C), modulation of the potential barrier extends through the entire grain volume, leading to a pronounced resistance variation and higher sensitivity.

Building on this mechanistic understanding, nanoscale engineering offers an effective route to amplify gas–solid interactions and charge modulation. Nanostructuring provides three main advantages: (i) a greatly enlarged surface area that increases the number of active adsorption sites, (ii) shortened carrier diffusion and transport pathways that accelerate response and recovery kinetics, and (iii) tunable porosity and inter-grain connectivity that improve charge-transfer efficiency and structural stability. These synergistic effects collectively enhance the chemical and electronic sensitivity of the sensing layer, enabling high performance even at reduced operating temperatures.

Among these factors, crystallite size reduction plays a particularly important role in strengthening surface-adsorption-driven charge modulation. When the crystallite diameter approaches or becomes smaller than twice the depletion width (Fig. 2b), the "small size effect" leads to full grain depletion, making even slight variations in surface charge produce pronounced resistance changes. These combined effects underpin the exceptional sensitivity of nanostructured gas sensors.

To utilize these advantages, researchers have designed nanostructures across different dimensionalities. Zero-dimensional (0D) nanoparticles maximize surface reactivity and quantum confinement effects, enabling rapid adsorption–desorption dynamics and pronounced resistance modulation (Fig. 2c and g).[37] When their characteristic size approaches the Debye length, adsorption-induced band modulation can extend through the entire nanoparticle volume, amplifying barrier/charge-carrier modulation beyond a near-surface shell. One-dimensional (1D) nanowires and nanotubes provide continuous electron-transport pathways and open diffusion channels, allowing fast sensor response and recovery with high signal stability (Fig. 2d and h).[38] The 1D backbone offers a low-discontinuity conduction route compared with particulate networks, while its open geometry shortens the diffusion distance for gas molecules to reach reactive sites. As a result, transduction kinetics are accelerated and cycle-to-cycle signal fluctuations are reduced. Two-dimensional (2D) materials, such as graphene and transition metal dichalcogenides (MoS_2 and WS_2), provide large specific surface areas and high carrier mobility, enabling low-temperature operation and, in some cases, room-temperature detection with excellent selectivity (Fig. 2e and i).[39] Because charge transport is confined to an ultrathin channel, adsorption-induced charge transfer can directly modulate carrier density and surface band bending, producing measurable conductance changes even at reduced operating temperatures. In addition, chemically/electronically distinct basal-plane *versus* edge/defect sites often lead to preferential adsorption and stronger charge perturbation for specific gas molecules, thereby improving selectivity. Three-dimensional (3D) hierarchical and porous architectures combine multiscale connectivity with large accessible pore volumes, supporting simultaneous adsorption and diffusion throughout the network and yielding robust, high-amplitude response signals (Fig. 2f and j).[40] The interconnected pore network increases gas-accessible surface while reducing diffusion tortuosity, thereby accelerating adsorption–desorption kinetics. In parallel, the continuous percolation framework provides multiple charge-transport pathways, mitigating bottlenecked conduction and improving signal robustness.

Overall, these dimension-tailored nanostructures illustrate how morphological engineering directly governs sensing kinetics, charge transport, and device-level performance. Accordingly, nanostructured architectures spanning 0D to 3D dimensions provide a practical design space to couple the intrinsic surface chemistry of MOS sensors with transport modulation within the sensing layer.

3. Wet-fabrication strategies for nanostructured gas sensors

Wet-chemical fabrication has become a key strategy for constructing nanostructured gas-sensing materials due to its flexibility, low cost, and compositional tunability. Unlike vapor-phase or lithographic routes, wet-fabrication relies on chemical control of nucleation and crystal growth in the liquid phase, enabling bottom-up formation of nanostructures with well-defined morphology and high crystallinity. By adjusting precursor concentration, pH, temperature, and reaction time, parameters such as grain size, porosity, and oxygen-vacancy distribution can be precisely tuned. These features are critical for MOS gas sensors, where surface reactivity, adsorption sites, and charge transport are closely related to nanostructural characteristics.[1,23] Moreover, solution-phase routes can produce stoichiometrically uniform, defect-controlled nanostructures that enhance reproducibility and operational stability and, in many cases, outperform conventional bulk or microstructured films.[41–43]

Hydrothermal synthesis is one of the most widely used wet-fabrication methods for creating high-quality nanostructures under mild conditions. In this process, the combination of temperature, pressure, and solvent composition determines dissolution, nucleation, and recrystallization behavior, allowing selective growth of specific crystal facets and highly crystalline products. Zhang *et al.* demonstrated this capability using a two-step hydrothermal strategy that integrates preformed ZnO nanorods with SnO_2 and reduced graphene oxide (rGO) into a hierarchical composite (Fig. 3a).[44] In the second hydrothermal step, SnO_2 crystallizes from Sn precursors while GO is reduced to rGO around the ZnO nanorods, yielding rGO-wrapped ZnO–SnO_2 aggregates that interconnect into a three-dimensional network with strong interfacial coupling (Fig. 3b).

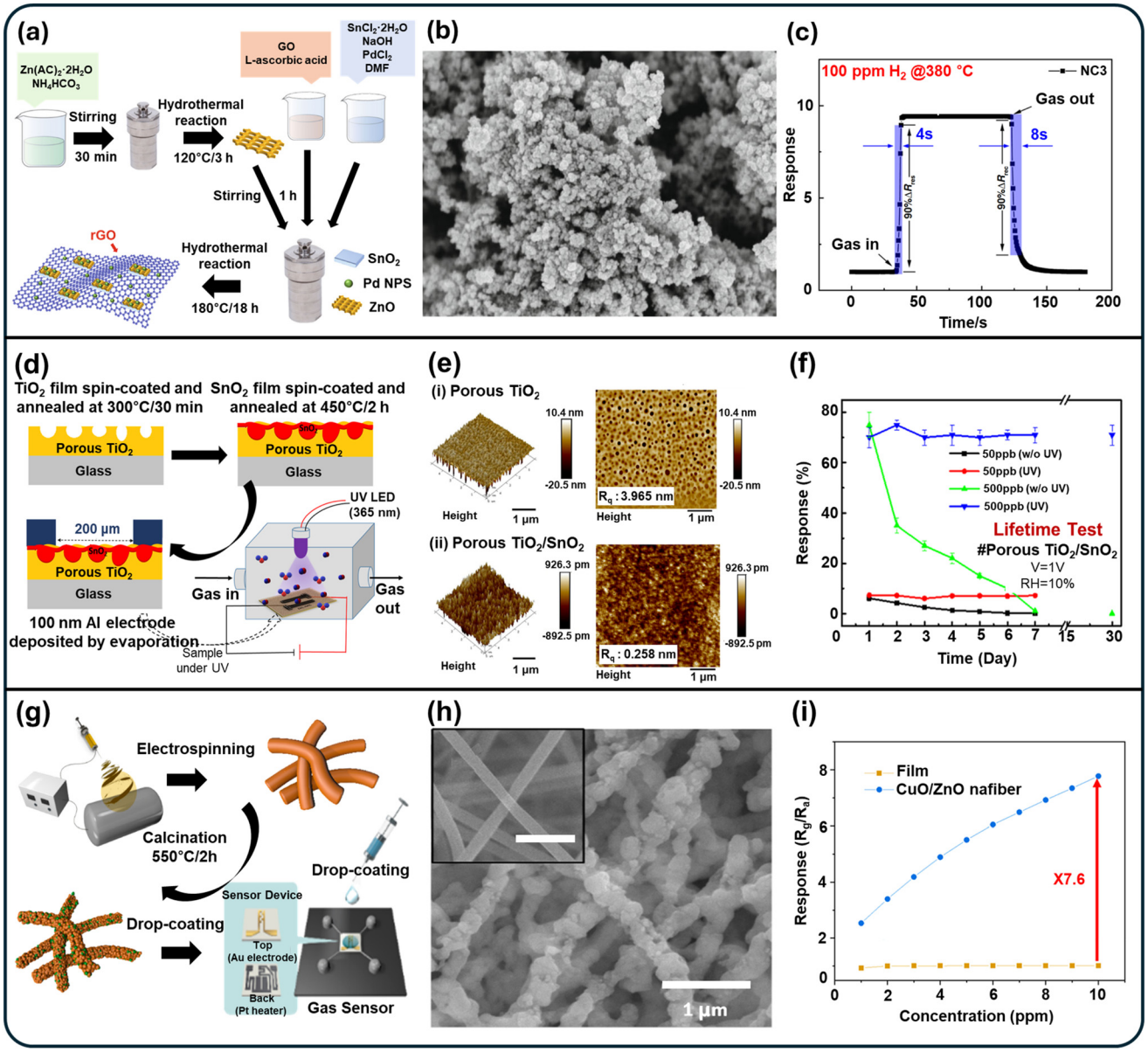

Fig. 3 Wet strategy for sensor fabrication, nanostructure, and sensing performance. (a) Schematic illustration of the fabrication of Pd-doped rGO/ZnO–SnO_2 nanocomposites *via* a hydrothermal route. (b) Scanning electron microscopy (SEM) image of hydrothermally derived rGO-supported ZnO–SnO_2 nanostructures. (c) H_2 (100 ppm, 280 °C) response–recovery curve exhibiting ultralow limit of detection (LOD) and fast kinetics enabled by the rGO/Pd–ZnO–SnO_2 synergy. (a–c) Adapted from ref. 44 Licensed under CC BY 4.0. (d) Schematic of the fabrication process of a porous TiO_2/SnO_2 sensor and the UV-illuminated measurement setup. (e) Atomic force microscopy (AFM) topography images (5 × 5 μm^2) of porous TiO_2, porous TiO_2/SnO_2, nonporous TiO_2, and nonporous TiO_2/SnO_2 thin films. (f) Long-term (30 days) stability comparison of the porous TiO_2/SnO_2 sensor with and without UV illumination. (d–f) Adapted from ref. 46 Licensed under CC BY 4.0. (g) Schematic illustration of the synthesis workflow and evaluation steps for the gas sensor. (h) SEM image of electrospun porous CuO/ZnO nanofibers. (i) Gas responses of CuO/ZnO nanofiber-based and film-type sensors toward 1–10 ppm C_2H_2. (g–i) Adapted with permission from ref. 42 Copyright 2024, American Chemical Society.

The rGO framework provides continuous conductive pathways and suppresses grain aggregation, while the oxide heterostructure enhances charge separation through continuous p–n–n junctions. As a result, the sensor exhibits an ultrafast response and recovery (4 s/8 s) and a low detection limit of 50 ppb toward H_2 at 380 °C (Fig. 3c). The excellent performance can be attributed to the large surface area and efficient modulation of the depletion region at nanoscale heterointerfaces, highlighting the importance of interface and defect engineering enabled by hydrothermal processing. In this architecture, nanoscale heterointerfaces serve as transduction sites where band alignment and local barrier modulation amplify the resistance response, while growth-associated defect states can increase adsorption activity and tune carrier density.

The sol–gel process provides another powerful wet-chemical route for fabricating nanostructured oxides with tunable poro-

sity and chemical composition.[45] This method involves hydrolysis and condensation of metal alkoxides or salts, forming a polymeric sol that transitions into a gel network and subsequently crystallizes upon heat treatment. Through careful control of precursor chemistry and solvent conditions, it is possible to obtain dense or porous nanostructures with uniform stoichiometry and adjustable pore architecture. Deb *et al.* fabricated a nanoporous TiO_2/SnO_2 nano-heterostructure using a two-step sol–gel method with a block-copolymer soft template, yielding an ordered porous network in which SnO_2 is embedded within a TiO_2 scaffold (Fig. 3d).[46] Atomic force microscopy (AFM) reveals a uniform sol–gel-derived film with interconnected nanopores, providing large accessible surface area and continuous pathways for gas diffusion (Fig. 3e). The resulting sensor delivers stable and reproducible NO_x detection at sub-ppm (ppb) levels for more than 30 days under very low-power UV photoactivation (Fig. 3f). The observed stability and repeatability are attributed to the regulated vacancy dynamics and conformal interface formation that minimize surface deactivation. In this context, vacancy-related states help sustain adsorption activity, and conformal interfaces reduce interfacial resistance drift, improving long-term signal reliability. This example highlights how sol–gel chemistry enables the molecular-level design of nanostructures with both mechanical stability and high surface reactivity.

Electrospinning is a versatile wet-fabrication technique capable of producing one-dimensional nanofibers with large specific surface area and high porosity.[47] In this process, a polymer–metal precursor solution is stretched under a strong electric field to form ultrafine fibers that solidify through solvent evaporation (Fig. 3g). Calcination converts these into nanocrystalline oxide fibers with interconnected grains and continuous charge-conduction pathways. This approach provides exceptional control over fiber diameter, crystallinity, and composition, while maintaining scalability for large-area production. Jung *et al.* synthesized a CuO/ZnO heterostructured nanofiber network by electrospinning followed by calcination, which exhibited a sevenfold enhancement in C_2H_2 sensitivity compared with a pristine ZnO film (Fig. 3h and i).[42] The fibrous architecture promotes efficient gas diffusion and adsorption due to its open network and nanoscale roughness. In addition, continuous CuO–ZnO p–n junctions distributed along the fiber axis facilitate charge separation and enhance modulation of the EDL. The built-in field at these junctions strengthens adsorption-induced barrier modulation. Meanwhile, defect- and vacancy-related sites in the nanocrystalline fiber network provide additional adsorption sites and locally tune carrier density, which supports rapid response and stable cycling behavior. The electrospun nanostructures also possess strong mechanical flexibility and stability, making them attractive for integration into flexible and large-area gas-sensing platforms.

Beyond these representative examples, wet-fabrication offers several overarching advantages for nanostructure engineering. The chemical tunability of the liquid phase allows control over defect concentration, doping level, and interfacial chemistry, enabling the design of sensors with optimized catalytic activity and carrier mobility. Wet processes also facilitate the incorporation of functional additives, such as graphene, noble-metal nanoparticles, or polymers, to improve sensitivity and selectivity toward specific gases.[48] Furthermore, the solution-based nature of these techniques supports large-area deposition on diverse substrates, including flexible or curved surfaces, which is particularly beneficial for emerging applications in environmental monitoring and portable electronics.[49] Recent developments in surfactant-assisted assembly, seed-mediated growth, and *in situ* templating have further expanded the structural complexity achievable through wet-chemistry, enabling hierarchical nanostructures that combine multiple dimensionalities and compositions in a single framework.

Overall, wet-fabrication techniques provide an indispensable platform for producing high-quality, compositionally controlled, and morphologically tunable nanostructures for gas-sensing applications. Their ability to simultaneously optimize crystallinity, porosity, and defect chemistry allows fine adjustment of the electronic and catalytic properties that dictate sensor performance. Such chemical-level control is also effective in regulating vacancy and defect states that govern adsorption energetics and carrier density, thereby influencing depletion-layer modulation during gas exposure. Furthermore, the same solution-phase tunability facilitates conformal interfacial chemistry and heterostructure formation in multicomponent architectures, which can promote more efficient charge transfer and strengthen signal transduction. As precursor design, reaction control, and self-assembly mechanisms continue to advance, wet-chemical routes will remain central to the development of next-generation nanostructured gas sensors that combine superior material quality with scalable synthesis and functional adaptability.

Nevertheless, translating wet-fabricated architectures into reproducible devices requires attention to several practical failure modes. Because many solution routes proceed in aqueous environments, the accessible material space can be constrained for compounds that are sensitive to water, which narrows the process window and limits material compatibility. In addition, subtle variations in reaction and post-annealing conditions can alter vacancy and defect states, thereby shifting adsorption energetics and carrier density and manifesting as baseline drift or sample-to-sample performance variations.

4. Dry-fabrication strategies for nanostructured gas sensors

While wet-chemical methods are effective for producing high-surface-area materials, their stochastic growth nature often leads to nonuniform structures and poor integration compatibility.[50–54] In contrast, dry-fabrication techniques based on vapor-phase deposition, lithographic patterning, and plasma processing offer precise control over geometry, film thickness, and interface quality.[55–59] These approaches enable

deterministic construction of nanostructures directly on device substrates while maintaining reproducibility and scalability essential for practical gas-sensor integration.[24,60,61]

A representative example of dry-process-based nanostructuring is the palladium nanowire hydrogen sensor developed by Kim *et al.* (Fig. 4a–c).[31] The key innovation in this work was

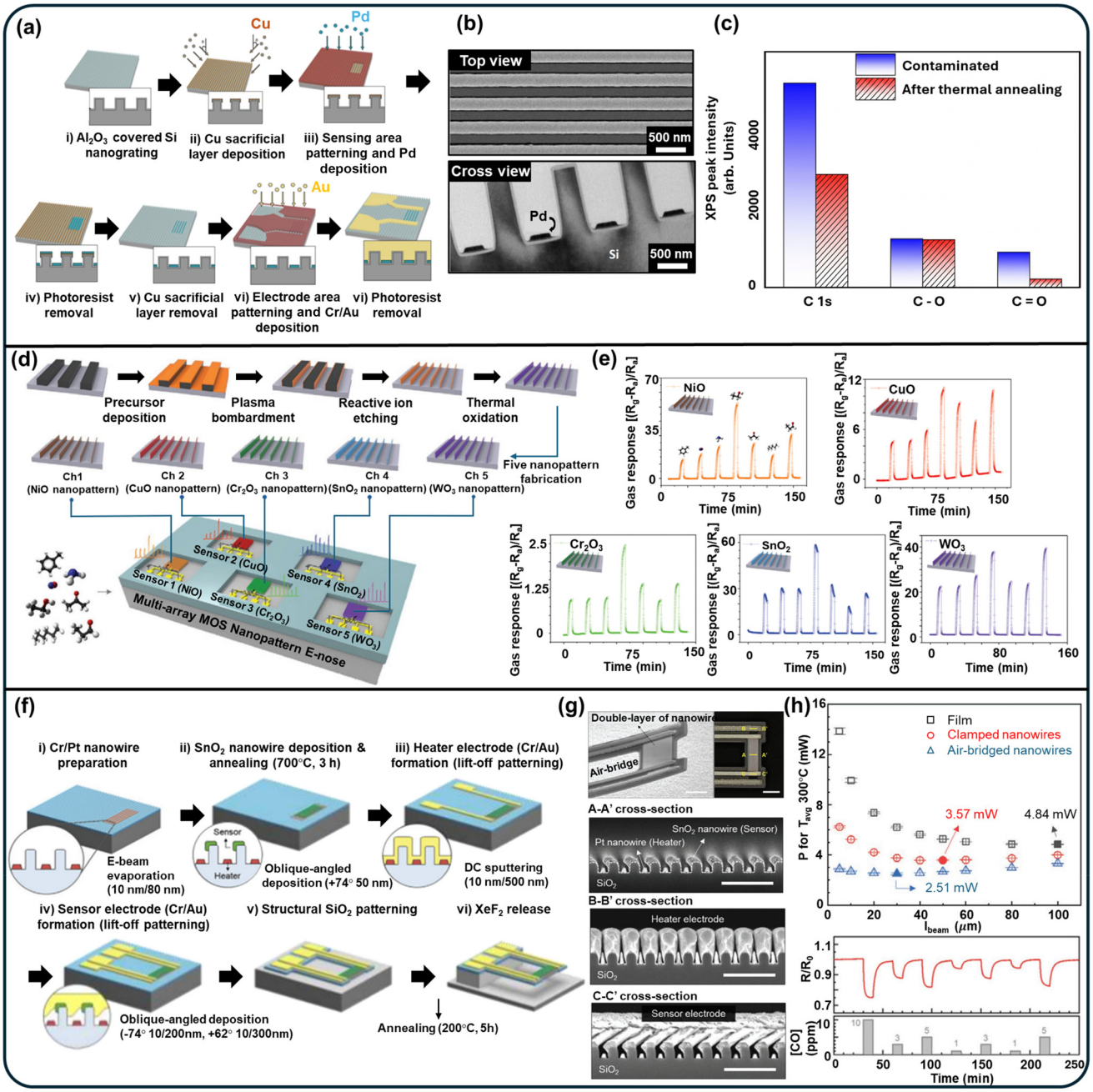

Fig. 4 Dry strategy for sensor fabrication, nanostructure, and sensing performance. (a) Schematic illustration of the fabrication process of a nanowire H_2 gas sensor. (b) Scanning electron microscopy (SEM) images in top view and cross-sectional view. (c) Chemo-electrical response of the as-fabricated sensor. (a–c) Reproduced from ref. 31 Licensed under CC BY-NC-ND 4.0. (d) Fabrication schematics of metal–oxide (NiO, CuO, Cr_2O_3, SnO_2, and WO_3) multi-array gas sensors with high-resolution nanopatterns achieved *via* low-energy plasma bombardment. (e) Sensing responses of the five nanopatterned channels; dynamic sensing responses of the NiO, CuO, Cr_2O_3, SnO_2, and WO_3 nanopatterned channels to seven different gases. (d and e) Adapted with permission from ref. 67 Copyright 2020, Wiley-VCH GmbH. (f) Schematics of the fabrication procedures, including detailed process conditions. (g) Projected-view SEM and top-view LSM images of the fabricated device with three sections highlighted in yellow, together with cross-sectional SEM images of the double-layer nanowires, heater electrode, and sensor electrode. (h) Transient response of the sensor resistance to various CO concentrations with the heater operating at 4.36 mW; gas responses compiled from five independent measurements, with the dashed line indicating the fitted sensitivity curve. (f–h) Adapted with permission from ref. 13 Copyright 2020, Wiley-VCH GmbH.

the use of a sacrificial shadow-mask layer formed *via* oblique-angle metal deposition, which enabled the definition of nanoscale Pd wires without any wet etching. By depositing a Cu sacrificial layer at an inclined angle, selective sidewall coverage was achieved through geometric shadowing. Subsequent normal-incidence deposition of Pd and removal of the Cu layer produced a precisely aligned Pd nanowire array on Si nanogratings (Fig. 4a and b). This dry, purely physical approach yielded well-ordered nanowires with high structural fidelity across the wafer, eliminating process variability associated with chemical patterning.[31,62,63] The nanoscale confinement realized through this method provides several critical advantages. The surface-to-volume ratio of Pd is greatly increased, facilitating rapid adsorption and desorption of hydrogen molecules, while the diffusion path for hydrogen atoms within the Pd lattice is shortened, accelerating hydride formation and decomposition.[31,64] These effects lead to faster response and recovery, as well as larger resistance modulation compared with planar Pd films. More importantly, this design addressed a major challenge in metal-based gas sensors—baseline drift caused by surface contamination. By integrating a microscale Joule heater directly beneath the Pd nanowires, the device enabled *in situ* surface regeneration through periodic thermal desorption of contaminants such as CO_2 and moisture (Fig. 4c). This self-refreshing mechanism effectively restored the initial baseline resistance and ensured consistent sensing over extended operation, offering a practical solution for long-term stability in dry-fabricated nanosensors.[31,65,66]

Building upon the concept of nanoscale confinement demonstrated in the Pd nanowire sensor, Kang *et al.*[67] advanced the dry-fabrication approach by employing plasma bombardment and directional etching to form high-aspect-ratio metal–oxide semiconductor (MOS) nanoribbons (Fig. 4d and e).[67] Thin precursor metal films were deposited and then sculpted into nanoscale ribbons through Ar^+ plasma bombardment and reactive-ion etching, followed by thermal oxidation to yield semiconducting oxides such as NiO, CuO, Cr_2O_3, SnO_2, and WO_3 (Fig. 4d).[12,67,68]

This plasma-assisted dry process enables material-independent patterning, allowing diverse MOS materials to be reproducibly converted into vertically confined nanoribbons with widths less than ~15 nm. The resulting structures exhibit complete carrier depletion and rapid gas diffusion, thereby amplifying the nanoscale effects realized in the nanowire device. The increased aspect ratio maximizes active surface area and enhances charge modulation, leading to high sensitivity and fast response (Fig. 4e).[67,69,70] Another critical advantage of this method is its wafer-scale reproducibility, which allows precise fabrication of multi-channel sensor arrays on a single chip. Each oxide nanoribbon provides a distinct response profile based on its surface chemistry and band structure, and their collective outputs form characteristic gas fingerprints for electronic-nose (E-nose) operation. The structural uniformity across the array minimizes baseline variations and improves the reliability of data-driven analysis such as principal component analysis (PCA), enabling clear discrimination among multiple analytes. Together with the previous sacrificial-mask-based Pd nanowire strategy, this plasma-etching approach demonstrates how dry-fabrication can further magnify nanoscale effects through high-aspect-ratio architectures and reproducible array formation—paving the way toward intelligent, large-scale gas-sensing systems.[67,71,72]

Finally, to overcome the persistent challenge of high power consumption in micro-hotplate-based MOS gas sensors, Choi *et al.*[13] introduced a suspended nanowire heater–sensor structure fabricated entirely *via* dry micromachining and angled vapor deposition (Fig. 4f–h). In this architecture, angled deposition was utilized to form nanogap arrays between adjacent Pt heater lines and SnO_2 sensing nanowires, effectively suppressing lateral heat conduction and improving thermal efficiency. Subsequently, XeF_2 isotropic dry etching was employed to remove the underlying Si substrate and suspend the entire oxide bridge structure in air (Fig. 4f and g).[13] This produced a freestanding nanowire network that exhibited strong thermal isolation, as heat was confined within the suspended region without dissipation into the bulk substrate.[30] The combination of nanoscale gaps and suspended geometry introduced a dual thermal confinement effect—minimizing heat loss while enabling localized, rapid heating of the active sensing area.[21,73–75] As a result, the device achieved stable CO detection down to 1 ppm at ~300 °C with total power consumption below 5 mW, representing over an order-of-magnitude improvement compared with conventional planar microheaters (Fig. 4h).[13] Beyond energy savings, the suspended configuration also enhanced mechanical stability and reduced stress accumulation due to its compliant nanowire-supported bridge design.[48,76,77] This example highlights how dry nanofabrication enables precise thermal engineering through geometric control, leveraging nanogap formation and nanoscale heat isolation to achieve ultra-efficient gas sensing.

Collectively, these three examples illustrate how dry-fabrication techniques have progressively evolved to address critical challenges in gas-sensor design—ranging from enhanced kinetics and stability (Pd nanowire), to selective and reproducible array integration (MOS nanoribbon), and finally to energy efficiency *via* nanoscale thermal isolation (suspended nanowire).[13,31,67] By uniting physical vapor processes, plasma-assisted patterning, and dry micromachining, these strategies establish a unified framework for precision control of morphology, material composition, and thermal management.[78] The geometric accuracy inherent to dry-fabrication allows structural tuning near the Debye length for optimal charge modulation, while wafer-level reproducibility and MEMS compatibility ensure scalability and integration with electronic systems.[48,79,80] Moreover, the solid-state nature of vapor-deposited materials provides mechanical robustness and high-temperature durability, enabling stable operation under harsh environmental conditions.[77,81,82] These advances position dry-fabricated nanostructures as a central design paradigm for next-generation gas sensors that are simultaneously sensitive, selective, power-efficient, and highly integrable.[13,30,80,83]

Despite these advantages, dry-fabricated sensing layers can also exhibit certain performance limitations. A common failure

Table 1 Comparison of fabrication strategies for nanostructured gas sensors. The table summarizes the general characteristics of wet- and dry-fabrication approaches in terms of crystallinity, structural control, integration compatibility, power consumption, and reproducibility/scalability

Fabrication method	Crystallinity	Structural control	Integration compatibility	Power consumption	Reproducibility and Scalability
Wet-fabrication (hydrothermal, sol–gel, electrospinning)	High (solution-phase crystal growth enables highly crystalline nanostructures)	Medium (high porosity and morphological versatility)	Low (direct growth on substrates with limited integration compatibility)	Low (possible room-temperature operation)	Medium (large-area synthesis with relatively low cost)
Dry-fabrication (sputtering, vapor deposition)	Medium (thin films may require post-annealing to improve crystallinity)	High (precise nanopatterning and uniform film thickness)	High (CMOS/MEMS compatible and suitable for wafer-level integration)	Medium (often requires microheaters with mW-level power consumption)	High (excellent wafer-scale reproducibility and batch processing)

mode of purely dry-processed sensing layers is reduced sensitivity and selectivity relative to wet-grown nanostructures. Relatively dense vapor-deposited films and lithographically patterned structures provide fewer accessible adsorption sites and limited surface tunability compared with solution-derived porous or hierarchical architectures, constraining both response magnitude and discriminability among interferent gases.

Considering these complementary strengths and limitations, wet- and dry-fabrication strategies involve important trade-offs between gas sensing performance and device manufacturability. Wet-chemical synthesis typically produces highly crystalline and porous nanostructures that offer enhanced sensitivity due to their large surface area and abundant adsorption sites. In contrast, dry-fabrication techniques provide superior structural precision, reproducibility, and compatibility with CMOS/MEMS platforms, enabling scalable device integration. These complementary characteristics are summarized in Table 1, which compares the key attributes of wet- and dry-fabrication approaches.

5. Hybrid dry–wet fabrication of gas sensors

The integration of dry- and wet-fabrication strategies has recently emerged as a promising pathway to overcome the trade-offs between structural precision and nanoscale reactivity in gas sensors.[84,85] Dry processing methods such as plasma etching, atomic layer deposition (ALD), and physical vapor deposition (PVD) ensure excellent control of geometry, reproducibility, and device integration, yet their films are often dense and chemically inert.[84,89] In contrast, wet synthesis approaches such as hydrothermal or sol–gel growth provide nanostructures with high surface area and abundant active sites but often suffer from weak adhesion and limited spatial control.[85,90,91] By combining these complementary routes, hybrid dry–wet fabrication enables the realization of architectures that integrate well-defined geometrical design with reactive nanostructured layers, achieving both device-level uniformity and surface-level functionality.[84,89,91]

A representative example highlights how spatially confined wet growth on dry-processed substrates enables uniform nanostructure formation with strong adhesion.[86] Liu *et al.* developed a design in which a MEMS-based micro-hotplate was prepatterned with electrodes and then coated with a porous polymer mask to confine solution precursors to defined sensing zones. During hydrothermal treatment, capillary forces concentrated the precursors within the template pores, promoting heterogeneous nucleation at electrode edges where surface energy was locally minimized (Fig. 5a). As the reaction proceeded, nanowalls self-assembled within the confined regions and coalesced into a continuous porous network anchored directly on the substrate. After the removal of the polymer mask, vertically aligned oxide nanowalls remained, exhibiting high uniformity and tight mechanical bonding (Fig. 5b). Electrical mapping across multiple devices showed nearly identical *I–V* characteristics, confirming that the addition of reactive oxide nanostructures did not compromise wafer-level reproducibility (Fig. 5c). This approach demonstrates that hybrid growth can introduce nanoscale porosity and high surface activity directly onto microheater platforms while preserving the integration precision of dry-processed devices.[97]

Liu *et al.* presented another example combining anisotropic dry etching with wet-chemical surface refinement to enhance charge transport.[87] In this case, aligned oxide channels were sculpted by anisotropic plasma etching, providing well-defined one-dimensional pathways for carrier conduction. The plasma etching ensured precise pitch and width control but inevitably introduced a thin surface layer rich in defects such as oxygen vacancies, dangling bonds, and chemisorbed oxygen species that trapped charge carriers. To recover the intrinsic conductivity of the oxide, a post-treatment using dilute KOH solution was applied (Fig. 5d). The wet-chemical etching selectively dissolved the amorphized regions generated by ion bombardment and simultaneously passivated residual trap sites. This gentle wet refinement not only smoothed the channel sidewalls but also lowered the interfacial potential barrier, resulting in significantly reduced resistance and improved linearity in current–voltage behavior (Fig. 5e). The outcome clearly demonstrated that coupling dry-defined alignment with wet-chemical healing can convert structural precision into electronic functionality, a critical step for achieving high signal-to-noise performance in nanostructured gas sensors (Fig. 5f).

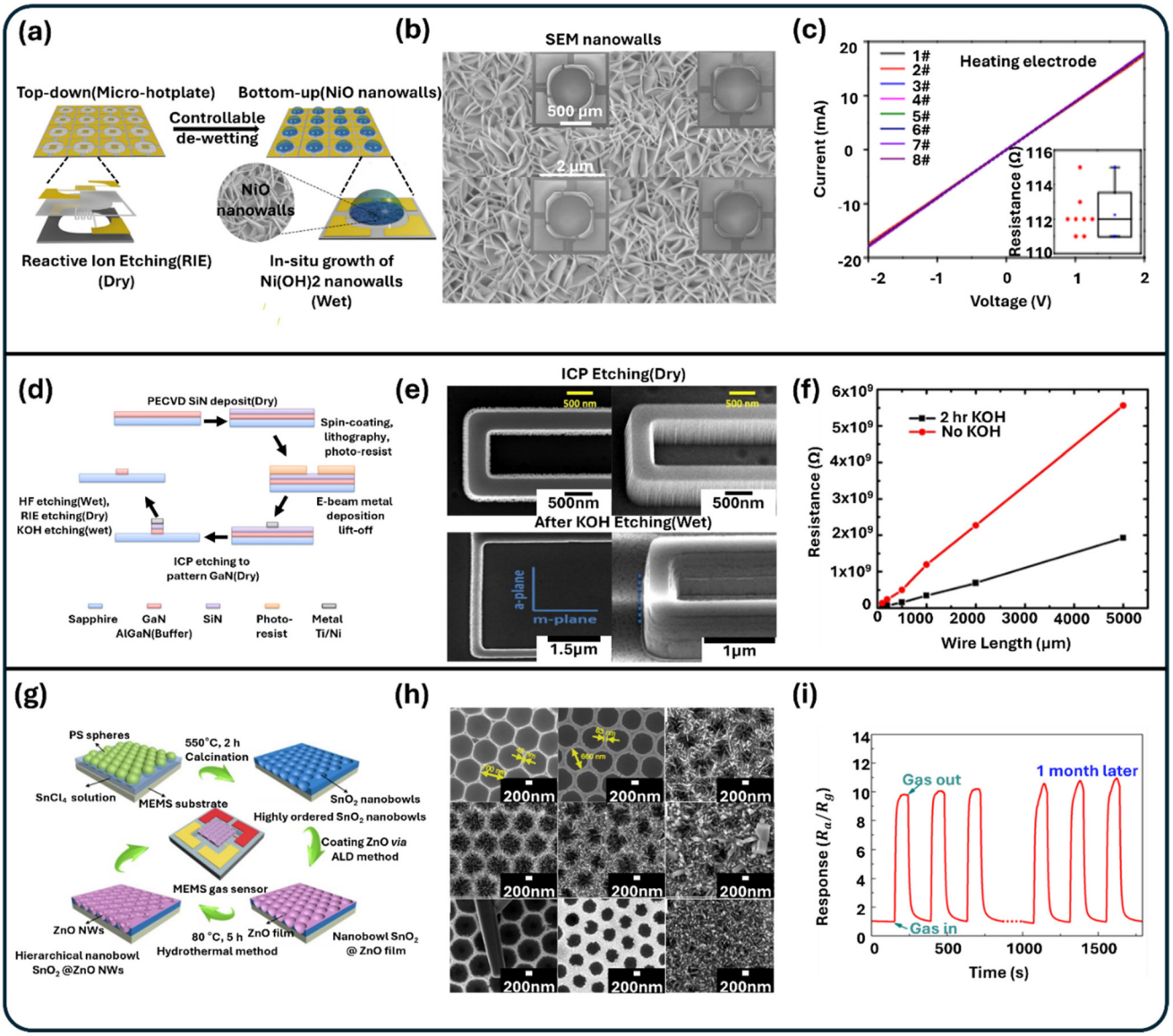

Fig. 5 Hybrid dry–wet strategy for sensor fabrication, nanostructure, and sensing performance. (a) Schematic of combined top-down and bottom-up fabrication for wafer-scale miniaturized gas sensors. (b) Scanning electron microscopy (SEM) images of sensors randomly chosen from the marked area of wafer-scale micro-hotplate. (c) *I*–*V* curves of heating electrodes of eight gas sensors from −2 V to 2 V (inset graph is the box chart of resistance of heating electrodes). (a–c) Adapted from ref. 86 Licensed under CC BY 4.0. (d) Schematic representation of the nanowire fabrication process flow. (e) SEM images of a nanowire section after ICP etch, shown in plan view (left) and 45° tilted view (right). (f) Electrical behavior with UV assistance of NW before and after KOH treatment. (d–f) Adapted with permission from ref. 87 Copyright 2015, Elsevier. (g) The synthetic protocol for the hierarchical highly ordered nanobowl SnO_2@ZnO NWs *in situ* on MEMS, combining a modified facile hard template method, an ALD process and a hydrothermal method. (h) SEM characterization of all the samples. (i) Long-term stability of the nanobowl SnO_2@ZnO NW gas sensor in air over one month. (g–i) Adapted from ref. 88 Licensed under CC BY 4.0.

Zhu *et al.* presented a third hybrid example illustrating how hierarchical nanostructures can be created through sequential dry and wet processes to enhance stability and sensitivity.[88] In this configuration, an ultrathin ALD seed layer was first conformally deposited onto a microstructured platform to define uniform nucleation sites with angstrom-level precision. The ALD process provided excellent conformality even on curved or recessed surfaces, ensuring complete coverage and strong adhesion. Subsequently, hydrothermal treatment was used to induce the growth of ZnO branches from the seeded surface, resulting in a multiscale SnO_2@ZnO network composed of interlinked nanosheets and nanorods. The ALD seed layer acted as both a diffusion barrier and an electron transport layer, while the ZnO branches provided high surface area and abundant adsorption sites (Fig. 5g). This multilevel hierarchy maximized the interaction between target gas molecules and the oxide surface while maintaining robust electrical connectivity to the underlying platform (Fig. 5h). Long-term stability

tests confirmed that the device maintained consistent baseline resistance and repeatable response even after extended exposure and thermal cycling, demonstrating that conformal ALD seeding followed by controlled hydrothermal branching effectively combines durability, adhesion, and high sensitivity within one architecture (Fig. 5i).

Collectively, these examples reveal the power of hybrid dry–wet fabrication to engineer nanostructures that integrate the strengths of both regimes. Dry processes define the mechanical framework and ensure electrical and thermal stability,[89,98] while wet synthesis imparts chemical reactivity, hierarchical porosity, and tunable defect chemistry.[99,100] By adjusting deposition thickness, etching anisotropy, and solution composition, hybrid dry–wet strategies can precisely tune active surface area, interfacial coupling, and carrier transport pathways. The resulting sensors exhibit faster response and recovery, lower operating temperature, and improved baseline retention compared to single-route devices.[89,99–101]

Beyond these case studies, hybrid dry–wet fabrication offers broad versatility for next-generation gas-sensing platforms. The compatibility of ALD, PVD, and plasma steps with low-temperature wet growth allows direct application to flexible or polymeric substrates, enabling roll-to-roll manufacturing and large-area conformal sensor networks.[102–104] Furthermore, combining oxide–oxide, oxide–2D, and oxide–polymer interfaces within hybrid architectures enables selective and multi-analyte detection suitable for electronic-nose (E-nose) arrays.[51,89] Integrated process control, such as *in situ* metrology and automated feedback during wet growth, can further stabilize nucleation and branching across wafer scales, promoting reproducibility and manufacturability. In addition to sensing performance, practical implementation of gas sensors also requires consideration of fabrication complexity and associated processing costs. In general, wet-chemical approaches rely on relatively simple processing and widely accessible equipment, whereas dry-fabrication routes enable wafer-level batch processing and high reproducibility once fabrication conditions are established. Hybrid dry–wet strategies can provide a balanced pathway by combining scalable device platforms with flexible material synthesis. In summary, hybrid dry–wet fabrication couples the deterministic structural control of dry processing with the chemical adaptability of wet synthesis, enabling scalable and high-performance nanostructured gas sensors. Through the rational combination of conformal seeding, surface refinement, and solution-phase assembly, this approach delivers architectures that simultaneously achieve precision, adhesion, and reactivity.[89,101] Such integration bridges the gap between nanoscale material design and functional device realization, offering a practical and scalable route toward reliable, energy-efficient, and high-sensitivity sensing systems for future environmental, industrial, and healthcare applications.[51,89,92,103,105]

Despite these advantages, hybrid dry–wet fabrication can introduce additional reliability challenges. For example, surface damage or exposed metal regions generated during dry processing may influence the kinetics of subsequent wet reactions and, in some cases, promote galvanic corrosion when dissimilar metals are present in electrolyte environments. This effect can lead to localized material degradation, structural thinning, or interfacial instability if not properly controlled. In addition, anisotropic or excessive wet etching may increase the risk of structural disconnection or morphological collapse, particularly when wet etching steps follow dry plasma processes. Therefore, careful co-optimization of dry processing conditions and wet-chemical parameters is necessary to maintain structural integrity and process reproducibility in hybrid dry–wet fabrication.

To provide a clearer overview of recent advances in nanostructured gas sensors, Table 2 summarizes the sensing performance of representative devices reported in recent literature. The table compiles key sensing parameters including sensing material, target gas, operating concentration range, sensing temperature, sensitivity, response and recovery time, and limit of detection (LOD). By comparing sensors fabricated through wet-, dry-, and hybrid dry–wet fabrication approaches, the table highlights how fabrication strategies influence sensing performance.

6. Application

Recent progress in nanoscale material design, hybrid device engineering, and AI-assisted signal interpretation has transformed gas-sensing technology.[106–109] The deliberate control of the nanostructure, combined with advances in miniaturization and data analytics, has enhanced intrinsic sensor performance in terms of sensitivity, selectivity, and stability while also expanding applicability to complex environments.[1,23,34,110] From optically driven intelligent sensors to flexible wearables, wireless freshness monitors, and energy-efficient industrial detectors, these developments share a common foundation in nanoscale structural engineering (Fig. 6).[111–114] The precise tuning of morphology, dimensionality, and surface chemistry not only improves gas–solid interactions and charge transport but also provides the physical basis that enables these new classes of applications.[34,115–118]

A representative example of this transition is the μLED-based photoactivated (μLP) nanosensor, which demonstrates how nanostructured architectures can directly translate into system-level intelligence (Fig. 6a–c).[107,111] An indium oxide (In_2O_3) sensing layer, fabricated *via* glancing-angle deposition, forms vertically aligned nanoporous columns with high surface-to-volume ratios that promote efficient photon absorption and rapid adsorption–desorption kinetics. The integration of a micro-LED beneath this porous nanostructure enables direct optical activation of the sensing layer without the need for external illumination (Fig. 6a and b). This configuration allows low-power operation, reducing energy consumption to the sub-milliwatt range while maintaining stable photoresponse.[111,119] Under dynamic light modulation, the sensor produces transient signals that encode gas-specific reaction kinetics. These time-dependent patterns, analysed

Table 2 Summary of representative recent gas sensors fabricated using wet-, dry-, and hybrid dry–wet fabrication strategies. The table compares key sensing parameters including sensing material, target gas, operating concentration range, sensing temperature, sensitivity, response/recovery time, and limit of detection (LOD), highlighting the performance characteristics of nanostructured gas sensors reported in recent studies

Fabrication method	Sensing material	Target gas	Concentration (ppm)	Sensing temperature (°C)	Sensitivity	Response/ recovery time	LOD (ppb)	Ref.
Wet	Pd-doped rGO/ZnO–SnO_2	H_2	50–500	380	9.4	4 s/8 s	50	44
Wet	CuO/ZnO	C_2H_2	1–10	200	7.6 (10 ppm)	—	—	42
Wet	CeO_2@rGO nanohybrid	NO_2	70	RT	52.84%	7 s/58 s	1 ppm	92
Wet	Au/SnO_2	H_2S	0.0005 (0.5 ppb)	RT	270%	30 s/126 s	2	93
Wet	Pt NPs@TiO_2–WO_3	NH_3	50	RT	92.28 (50 ppm)	23 s/8 s	75	94
Wet	VO_2(A) nanowires	H_2S	0.5–10	RT	2.09 (10 ppm)	11 s/387 s	500	95
Wet	$FeVO_4$ nanofibers	*n*-Butanol	10–100	300	4.05	3 s/14 s	8.6 ppm	96
Dry	Pd nanowire	H_2	0.1–4%	RT	10–17%	<25 s	1000 ppm	31
Dry	NiO	C_2H_5OH	5	300	60.35	<5 min/<15 min	—	67
Dry	CuO	C_2H_5OH	5	300	11.67	<5 min/<15 min	—	67
Dry	Cr_2O_3	C_2H_5OH	5	300	2.44	<5 min/<15 min	—	67
Dry	SnO_2	C_2H_5OH	5	300	58.46	<5 min/<15 min	—	67
Dry	WO_3	C_3H_6O	5	300	39.45	<5 min/<15 min	—	67
Dry	SnO_2	CO	1–10	300	5–28%	—	1 ppm	13
Dry	SnO_2	CO	1–30	300	5–15%	15 s/50 s	1 ppm	30
Dry	Pd nanowire	H_2	0.1–10%	65	6%	<1 s/<2 s	0.1%	77
Dry	SnO_2 nanowire	CO	1–30	300	20.1%	17 s/77 s	1 ppm	21
Hybrid dry–wet	NiO	H_2S	0.3–50	200	1.5 (5 ppm)	—	—	60
Hybrid dry–wet	GaN	—	—	RT	—	—	—	87
Hybrid dry–wet	SnO_2	H_2S	1	250	6.24 (1 ppm)	14 s/39 s	1000	88
Hybrid dry–wet	SnO_2	C_2H_5OH	0.02	350	1.06 (0.02 ppm)	2 s/2 s	20	72

using deep convolutional neural networks, enable accurate classification of multiple gases and even mixed analytes within seconds.[111,120] The combination of optical control, porous nanostructure, and machine-learning analysis highlights how nanoscale morphology determines both energy efficiency and data richness (Fig. 6c). This architecture provides a scalable foundation for applications such as wearable diagnostics, air-quality management, and distributed environmental monitoring, where compact, intelligent sensing modules are required.

Building on this concept of nanoscale-enabled intelligence, the extension of nanostructured sensors into flexible and deformable architectures has opened a path toward wearable and conformal devices.[112,121–123] Conventional metal oxide sensors exhibit excellent chemical stability but are brittle and difficult to integrate with flexible substrates.[124,125] To address this limitation, Han *et al.* developed an all-inorganic flexible chemiresistor (ZIC sensor) that achieves mechanical durability and electrical stability through structural design at the nanoscale.[112] The device is built on a fibrous yttria-stabilized zirconia (YSZ) substrate coated with an ultrathin In_2O_3/g-C_3N_4 heterostructure. The nanofiber network distributes strain uniformly during bending and twisting, while maintaining electron transport paths across the structure. This morphology prevents stress concentration and cracking, ensuring stable resistance values even under repeated deformation (Fig. 6d and e). Furthermore, the heterointerface between the oxide and nitride layers enhances charge transfer and enables visible-light-driven operation at room temperature. These features together allow reliable gas detection during motion, establishing the feasibility of on-body sensing. The ZIC sensor demonstrates that nanoscale structuring can simultaneously provide mechanical flexibility, photoactivity, and environmental robustness, enabling continuous gas detection in wearable and portable systems (Fig. 6f and g).

The versatility of nanostructured materials is further exemplified in real-time food-freshness monitoring systems that integrate sensing and communication functions.[126–129] Sonwal *et al.* reported a hierarchical WS_2/reduced graphene oxide (rGO) composite sensor capable of detecting trace ammonia, a key indicator of meat spoilage, at room temperature (Fig. 6h).[113] The hybrid nanostructure, synthesized *via* a single-step hydrothermal method, combines the high carrier mobility of rGO with the sulfur-rich, catalytically active edges of WS_2. This architecture forms a porous p–p heterojunction with abundant adsorption sites, enabling fast charge transfer and selective interaction with ammonia molecules. The open network facilitates rapid molecular diffusion, yielding sub-ppb detection limits without external heating. When connected to a Bluetooth Low Energy (BLE) communication module, the sensor transmits data to a cloud-based platform for continuous freshness monitoring (Fig. 6i). During practical testing with beef samples, resistance increased consistently with spoilage progression, correlating well with ammonia release (Fig. 6j). This demonstration illustrates how nanostructured heteromaterials can merge high sensitivity with digital integration, allowing real-time, networked monitoring of perishable goods. The WS_2/rGO composite system highlights the adaptability of wet-synthesized nanostructures to scalable IoT applications and provides a foundation for smart packaging and distributed food-safety networks.

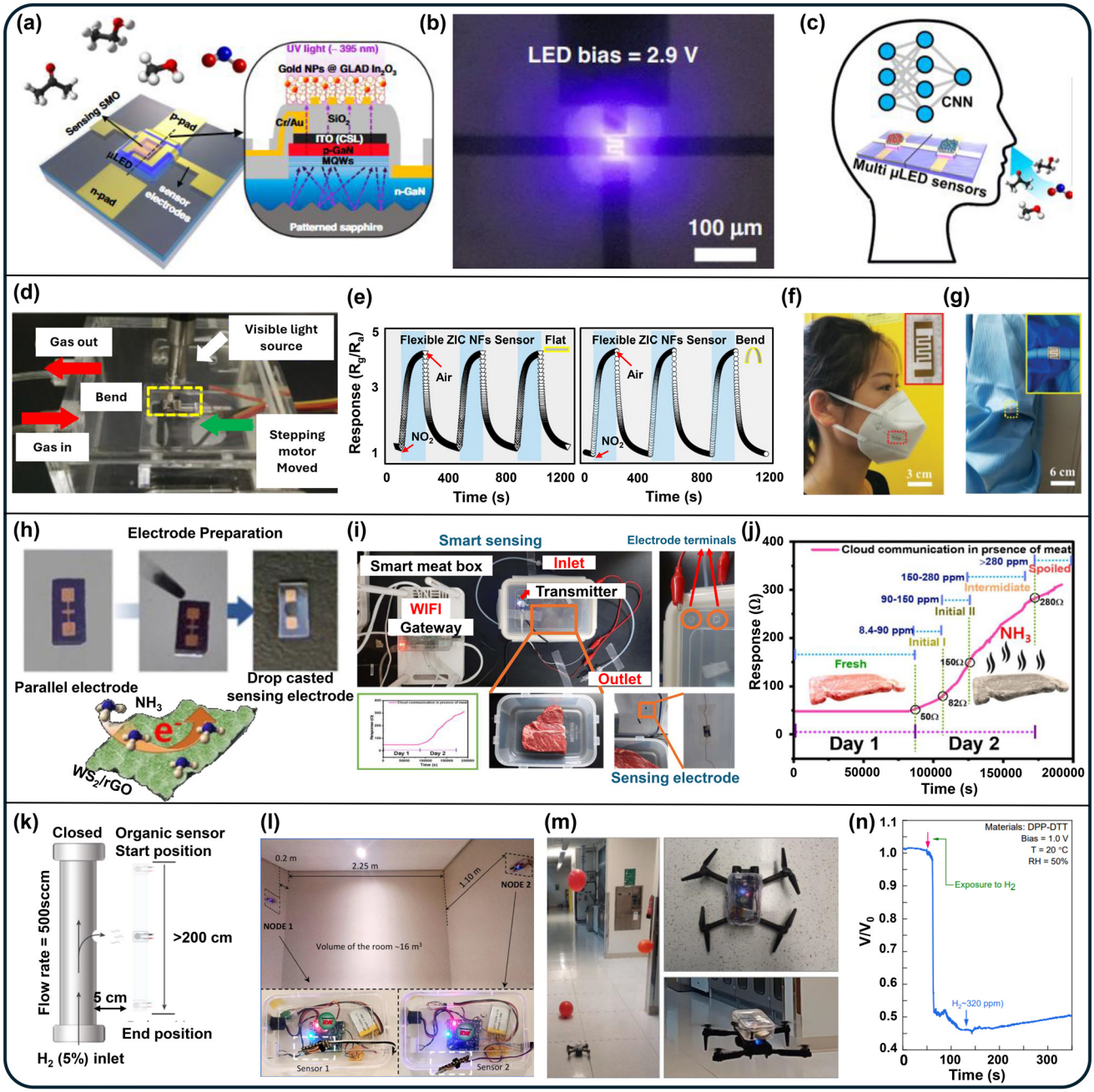

Fig. 6 Applications: e-nose, wearable platforms, food-spoilage monitoring, and industrial H_2 leak detection. (a) Schematic illustration of a micro-LED (μLED)-embedded photoactivated (μLP) gas sensor device. (b) Optical microscopic images of the fabricated sensor and the near-ultraviolet μLED (λ_{peak} = 395 nm, forward bias = 2.9 V). (a and b) Adapted from ref. 111 Licensed under CC BY 4.0. (c) μLED gas sensor interfaced with a CNN for odor classification. Adapted with permission from ref. 119 Copyright 2022, American Chemical Society. (d) Photograph of the ZIC NF sensor with Au interdigital electrodes. (e) Electrical connection performance test of the ZIC sensor under repeated folding. (f) Photograph of the ZIC NF sensor on the surface of a 3M mask. (g) Photograph of the ZIC NF sensor on the surface of experimental clothing under bending. (d–g) Adapted from ref. 112 Licensed under CC BY 4.0. (h) Electrode preparation by drop-casting a sulfur-rich WS_2/rGO composite over the Au interdigitated electrode gap. (i) Schematic representation of a real-time meat spoilage monitoring setup. (j) Real-time gas-sensing responses *via* a cloud communication system in the absence and presence of meat. (h–j) Adapted from ref. 113 Licensed under CC BY-NC 3.0. (k) Schematic illustration of the measurement setup of a H_2 leak detection system, where an organic sensing unit is moved slowly towards the hydrogen-exposed region to detect the hydrogen concentration leaking from a pipe carrying hydrogen gas; the data are wirelessly transmitted to a smartphone. (l) Photograph of the experimental setup used for wireless monitoring of H_2 concentration inside a closed room, where two sensing nodes (Node 1 and Node 2) are installed on opposite walls. (m) Organic hydrogen-sensing system deployed on a drone to monitor the hydrogen concentration generated from a bursting H_2-filled balloon (left); photographs of the organic sensing system mounted on the drone for environmental surveillance at rest (top right) and during flight (bottom right). (n) Time-dependent normalized voltage variation when the drone-mounted sensor node passes through the part of the corridor containing leaked hydrogen (simulated by bursting an H_2-filled balloon). (k–n) Adapted from ref. 114 Licensed under CC BY 4.0.

The role of nanostructure becomes even more critical in ultra-low-power hydrogen detection for industrial safety.[77,130,131] Hydrogen's high flammability and fast diffusion require continuous monitoring at low concentrations and ambient temperatures.[132–135] Conventional oxide-based sensors typically rely on high-temperature operation, which increases power consumption and limits stability.[114,136–139] Mandal *et al.* addressed these challenges using a DPP-DTT-based organic semiconductor, which was deposited as a thin nanostructured film on platinum electrodes.[114] The film's controlled nanomorphology provides efficient gas permeability and short diffusion paths, while the catalytic activity of platinum enables the dissociation of hydrogen into atomic species. Upon hydrogen exposure, atomic hydrogen reacts with oxygen dopants in the polymer, reversing the p-doping and reducing current. This process results in a strong, rapid response with sub-second reaction times and ppb-level detection limits at power levels below 2 μW. The device maintains stability across wide temperature and humidity ranges and shows reliable long-term operation exceeding 600 days. When integrated with wireless modules, multiple sensors can be distributed in confined spaces for real-time monitoring, and drone-mounted versions allow mobile detection of hydrogen leaks (Fig. 6k–n). These results demonstrate how controlled nanoscale morphology and catalytic interfaces enable both high performance and system-level integration in safety-critical environments.

Collectively, these applications reveal how the deliberate design of nanostructure transforms gas sensors from simple detectors into multifunctional, adaptive systems. In each case, nanostructural control enhances reactivity, accelerates charge transport, and stabilizes performance, which in turn enables operation in previously inaccessible regimes of flexibility, power efficiency, or selectivity. The μLP sensor achieves intelligent gas recognition through optically active nanocolumns, the ZIC sensor attains mechanical reliability through nanofiber architectures, the WS_2/rGO composite translates chemical sensitivity into networked data through porous 2D interfaces, and the DPP-DTT system realizes ambient, ultra-low-power hydrogen detection through nanoscale organic design.[111–114] These examples collectively show that nanostructured engineering is not merely an optimization tool but the enabling foundation that allows gas sensors to extend into intelligent, autonomous, and connected domains.[111,120,140]

In summary, the expanding application space of gas sensors is rooted in advances in nanostructure design.[1,2,34,122,141] Precise control over morphology, interfacial chemistry, and dimensionality has yielded sensors with exceptional sensitivity, selectivity, and stability. These intrinsic improvements now support deployment across a broad range of fields, including wearable health monitoring, smart packaging, environmental analysis, and industrial safety. As nanoscale architectures continue to evolve, gas sensors are poised to become fundamental components of intelligent systems, bridging material innovation with digital functionality and enabling a future where sensing and information processing are seamlessly integrated into everyday environments.[1,3,108,142–145]

7. Conclusion

The development of gas sensors has progressed beyond simple material substitution toward the deliberate engineering of nanostructures that couple morphology, surface chemistry, and device architecture. Through precise control of these parameters, nanostructured architectures have transformed conventional chemiresistors into adaptive and multifunctional systems capable of meeting modern demands for sensitivity, selectivity, stability, and scalability. The convergence of nanoscale design with advanced fabrication and intelligent data interpretation now enables devices that operate efficiently under low power while maintaining high analytical fidelity. To translate laboratory-level performance into field-grade reliability, failure-mode-driven design should accompany nanostructure engineering, explicitly accounting for baseline drift, electronic noise, and humidity susceptibility under long-term operation.

Each fabrication strategy offers unique advantages in the design of nanostructured gas sensors. Fabrication techniques fundamentally determine key sensing figures of merit by controlling accessible surface area, gas-diffusion pathways, defect chemistry, and electronic states within the sensing layer. These structural and electronic characteristics govern sensitivity and detection limits through adsorption capacity and charge-transfer modulation, while response and recovery kinetics are influenced by mass transport and reaction rates in the engineered nanostructure. In addition, the device architecture and thermal/electrical design enabled by fabrication processes strongly affect power consumption and operational stability. For practical deployment, scalable translation also requires standardized reliability metrics, including drift rate, hysteresis, poisoning tolerance, and device-to-device variability under realistic mixed-gas environments. In this context, dry-fabrication processes provide excellent dimensional precision and integration compatibility, enabling reproducibility and wafer-level manufacturability. In contrast, wet-chemical synthesis offers greater morphological flexibility and rich surface chemistry, producing highly porous structures and tunable defect states that enhance gas–solid interactions. Consequently, hybrid dry–wet fabrication strategies have emerged as a promising pathway that combines the structural precision of dry processing with the chemical functionality of wet synthesis. By integrating these complementary advantages, hybrid approaches enable well-integrated, porous, and stable sensing layers, helping bridge the gap between laboratory-scale demonstrations and deployable wafer-level sensor arrays.

At the material level, advances in hierarchical metal oxides, two-dimensional hybrids, and organic semiconductors have expanded operational boundaries from high-temperature systems to ambient and flexible platforms. Integration of photo-activation, microheating, and artificial intelligence-based analytics is redefining how gas sensors process information, converting transient electrical responses into interpretable data streams. In this context, information-rich transient signatures such as dynamic resistance trajectories and recovery kinetics can be treated as fingerprints and analyzed

using machine-learning-based analytics for reliable identification in complex mixed-gas environments. As a result, gas sensors are evolving from static detectors into intelligent and context-aware devices capable of autonomous decision-making. Accordingly, research is expected to expand from single-sensor outputs to electronic-nose platforms that combine sensor arrays with algorithmic decision layers for real-world discrimination.

Looking ahead, the trajectory of gas-sensing research is expected to emphasize scalability, intelligence, and integration. Future directions will focus on physics-informed design based on Debye-length-aware geometries and real-time feedback for process control, reconfigurable and hierarchical architectures that combine conformal seeding with programmable nucleation, and energy-efficient operation through hybrid photo-thermal activation and local computation. Parallel efforts will aim to establish standardized datasets and interoperable frameworks to enhance algorithmic selectivity and trustworthy deployment across diverse environments. Standardized datasets should therefore include raw transient responses together with environmental metadata, enabling uncertainty-aware learning and more trustworthy deployment across diverse field conditions. Together, these directions reflect a shift from isolated sensor development toward comprehensive sensing networks that merge physical detection with digital intelligence.

In summary, nanostructured gas sensors represent a new paradigm in which material design, fabrication, and computation form a unified framework. As the field continues to advance toward CMOS-compatible, data-driven, and self-sustaining platforms, nanostructured sensing will underpin the next generation of intelligent, networked systems for environmental monitoring, healthcare, industrial safety, and beyond. By integrating reliability engineering, standardized evaluation, scalable hybrid manufacturing, and interpretable AI analytics, future gas-sensing technologies can progress from high-performing single devices to deployable, trustworthy sensor networks operating in complex real-world environments.

Author contributions

J.-A. J., S.-J. P., H.-J. K, S. M. W. and J.-Y. Y. wrote the original draft. J.-A. J., S.-J. P., H.-J. K, G. L., S. M. W. and J.-Y. Y. conceptualized, supervised, and edited the draft. All authors participated in scientific discussion.

Conflicts of interest

There are no conflicts to declare.

Data availability

No primary research results, software or code have been included and no new data were generated or analysed as part of this review.

Acknowledgements

J.-Y. Y. acknowledges funding from the Basic Research Laboratory (BRL) Project of the National Research Foundation (RS-2024-00406674) funded by the Ministry of Science and ICT of Korea, as well as the Technology Innovation Program (RS-2024-00443121) funded by the Ministry of Trade Industry and Energy (MOTIE, Korea). This work was supported by the Korea Planning & Evaluation Institute of Industrial Technology (RS-2024-00427006).

References

1 P. K. Panigrahi, B. Chandu and N. Puvvada, *ACS Omega*, 2024, **9**, 3092–3122.
2 X. Chen, M. Leishman, D. Bagnall and N. Nasiri, *Nanomaterials*, 2021, **11**, 1927.
3 S. Hooshmand, P. Kassanos, M. Keshavarz, P. Duru, C. I. Kayalan, İ. Kale and M. K. Bayazit, *Sensors*, 2023, **23**, 8648.
4 U. Chakraborty, A. Kaushik, G. R. Chaudhary and Y. K. Mishra, *Curr. Opin. Environ. Sci. Health*, 2024, **37**, 100532.
5 S. Cui, H. Pu, S. A. Wells, Z. Wen, S. Mao, J. Chang, M. C. Hersam and J. Chen, *Nat. Commun.*, 2015, **6**, 8632.
6 W. Y. Chen, X. Jiang, S.-N. Lai, D. Peroulis and L. Stanciu, *Nat. Commun.*, 2020, **11**, 1302.
7 T. Tian, H. Yin, L. Zhang, M. Zhu, D. Ma, F. Shao, N. Hu, Z. Yang, Y. Zhang and Y. Su, *Appl. Surf. Sci.*, 2023, **609**, 155357.
8 M. A. Belal, S. Hajra, S. Panda, K. R. Kaja, M. M. M. Abdo, A. Abd El-Moneim, D. Janas, Y. K. Mishra and H. J. Kim, *J. Mater. Chem. A*, 2025, **13**, 5447–5497.
9 R. Thayil and S. R. Parne, *J. Mater. Sci.: Mater. Electron.*, 2025, **36**, 322.
10 R. Thayil and S. R. Parne, *J. Electron. Mater.*, 2026, **55**, 278–286.
11 R. Thayil and S. R. Parne, *Chem. Pap.*, 2025, 1–8.
12 W. B. Jung, S. Jang, S. Y. Cho, H. J. Jeon and H. T. Jung, *Adv. Mater.*, 2020, **32**, 1907101.
13 K. W. Choi, M. S. Jo, J. S. Lee, J. Y. Yoo and J. B. Yoon, *Adv. Funct. Mater.*, 2020, **30**, 2004448.
14 D. A. Dudorova, T. L. Simonenko, N. P. Simonenko, P. Y. Gorobtsov, I. A. Volkov, E. P. Simonenko and N. T. Kuznetsov, *Molecules*, 2023, **28**, 2515.
15 Y. Tao and P. P. Pescarmona, *Catalysts*, 2018, **8**, 212.
16 C. Xiang, T. Chen, Y. Zhao, J. Sun, K. Jiang, Y. Li, X. Zhu, X. Zhang, N. Zhang and R. Guo, *Nanomaterials*, 2022, **12**, 2133.
17 Z. Fan, D. Cui, Z. Zhang, Z. Zhao, H. Chen, Y. Fan, P. Li, Z. Zhang, C. Xue and S. Yan, *Nanomaterials*, 2020, **11**, 41.
18 L.-W. Mao, L.-Y. Zhu, T. T. Wu, L. Xu, X.-H. Jin and H.-L. Lu, *Appl. Surf. Sci.*, 2022, **602**, 154339.
19 J. W. Baek, E. Shin, J. Lee, D.-H. Kim, S.-J. Choi and I.-D. Kim, *ACS Sens.*, 2024, **10**, 33–53.

20 L. D'Arsié, V. Alijani, S. S. Brunelli, F. Rigoni, G. Di Santo, M. Caputo, M. Panighel, S. Freddi, L. Sangaletti and A. Goldoni, *Sci. Rep.*, 2018, **8**, 10028.
21 M.-S. Jo, S.-H. Kim, S.-Y. Park, K.-W. Choi, S.-H. Kim, J.-Y. Yoo, B.-J. Kim and J.-B. Yoon, *ACS Sens.*, 2024, **9**, 1896–1905.
22 J.-S. Jang, S. Qiao, S.-J. Choi, G. Jha, A. F. Ogata, W.-T. Koo, D.-H. Kim, I.-D. Kim and R. M. Penner, *ACS Appl. Mater. Interfaces*, 2017, **9**, 39464–39474.
23 N. Chowdhury and B. Bhowmik, *Nanoscale Adv.*, 2021, **3**, 73–93.
24 N. Kaur, M. Singh and E. Comini, *Langmuir*, 2020, **36**, 6326–6344.
25 A. Imash, G. Smagulova, B. Kaidar, A. Keneshbekova, R. Kazhdanbekov, L. F. Velasco and Z. Mansurov, *Sensors*, 2024, **24**, 6797.
26 K. Lang, T. Liu, D. J. Padilla, M. Nelson, C. W. Landorf, R. J. Patel, M. L. Ballentine, A. J. Kennedy, W.-S. Shih and A. Scotch, *Adv. Sens. Energy Mater.*, 2024, **3**, 100093.
27 A. Bag and N.-E. Lee, *J. Mater. Chem. C*, 2019, **7**, 13367–13383.
28 Y. Liu, X. Li, X. Li, C. Shao, C. Han, J. Xin, D. Lu, L. Niu, Y. Tang and Y. Liu, *Sens. Actuators, B*, 2022, **365**, 131926.
29 D. Zhang, N. Luo, Z. Xue, Y. Bai and J. Xu, *Talanta*, 2024, **274**, 125995.
30 S. H. Kim, M. S. Jo, K. W. Choi, J. Y. Yoo, B. J. Kim, J. S. Yang, M. K. Chung, T. S. Kim and J. B. Yoon, *Small*, 2024, **20**, 2304555.
31 K.-H. Kim, M.-S. Jo, S.-H. Kim, B. Kim, J. Kang, J.-B. Yoon and M.-H. Seo, *Nat. Commun.*, 2024, **15**, 8761.
32 W. Quan, J. Shi, H. Luo, C. Fan, W. Lv, X. Chen, M. Zeng, J. Yang, N. Hu and Y. Su, *ACS Sens.*, 2023, **8**, 103–113.
33 H.-J. Kim and J.-H. Lee, *Sens. Actuators, B*, 2014, **192**, 607–627.
34 Y.-F. Sun, S.-B. Liu, F.-L. Meng, J.-Y. Liu, Z. Jin, L.-T. Kong and J.-H. Liu, *Sensors*, 2012, **12**, 2610–2631.
35 A. Rothschild and Y. Komem, *J. Appl. Phys.*, 2004, **95**, 6374–6380.
36 N. Barsan, C. Simion, T. Heine, S. Pokhrel and U. Weimar, *J. Electroceram.*, 2010, **25**, 11–19.
37 K. Wu, W. Zhang, Z. Zheng, M. Debliquy and C. Zhang, *Appl. Surf. Sci.*, 2022, **585**, 152744.
38 P. R. Godse, S. A. Kadam, T. M. Nimbalkar, Y. M. Jadhav, Y. B. Jadhao, Y.-R. Ma and V. B. Patil, *Mater. Adv.*, 2024, **5**, 2826–2840.
39 Z. Li, Z. Lin, N. Wang, J. Wang, W. Liu, K. Sun, Y. Q. Fu and Z. Wang, *Sens. Actuators, B*, 2016, **235**, 222–231.
40 J. Wu, Z. Wu, H. Ding, Y. Wei, W. Huang, X. Yang, Z. Li, L. Qiu and X. Wang, *Sens. Actuators, B*, 2020, **305**, 127445.
41 T. Zhou and T. Zhang, *Sens. Actuators, B*, 2022, **371**, 132565.
42 M.-H. Jung, M. Kwak, J. Ahn, J.-Y. Song, H. Kang and H.-T. Jung, *ACS Sens.*, 2024, **9**, 217–227.
43 M. A. Andio, P. N. Browning, P. A. Morris and S. A. Akbar, *Sens. Actuators, B*, 2012, **165**, 13–18.
44 X. Zhang, J. Sun, K. Tang, H. Wang, T. Chen, K. Jiang, T. Zhou, H. Quan and R. Guo, *Microsyst. Nanoeng.*, 2022, **8**, 67.
45 M. Ben Arbia, H. Helal and E. Comini, *Nanomaterials*, 2024, **14**, 359.
46 M. Deb, Y. Ghossoub, L. Noel, P.-H. Li, H.-Y. Tsai, O. Soppera and H.-W. Zan, *ACS Appl. Mater. Interfaces*, 2025, **17**, 14670–14681.
47 H. Chen, H. Chen, J. Chen and M. Song, *Sensors*, 2024, **24**, 2962.
48 M. H. Seo, J. Y. Yoo, M. S. Jo and J. B. Yoon, *Adv. Mater.*, 2020, **32**, 1907082.
49 B. Aydas, A. Atılgan, A. Ajjaq, S. Acar, M. F. Öktem and A. Yildiz, *Ceram. Int.*, 2024, **50**, 32477–32489.
50 J.-K. Ko, I.-H. Park, K. Hong and K. C. Kwon, *Nanomaterials*, 2024, **14**, 1397.
51 P. M. Bulemo, D.-H. Kim, H. Shin, H.-J. Cho, W.-T. Koo, S.-J. Choi, C. Park, J. Ahn, A. T. Guntner and R. M. Penner, *Chem. Rev.*, 2025, **125**, 4111–4183.
52 M. Akbari-Saatlu, M. Procek, C. Mattsson, G. Thungström, H.-E. Nilsson, W. Xiong, B. Xu, Y. Li and H. H. Radamson, *Nanomaterials*, 2020, **10**, 2215.
53 X. Li, L. Fu, H. Karimi-Maleh, F. Chen and S. Zhao, *Heliyon*, 2024, **10**, e27740.
54 Y. Jian, W. Hu, Z. Zhao, P. Cheng, H. Haick, M. Yao and W. Wu, *Nano-Micro Lett.*, 2020, **12**, 71.
55 C. Marichy and N. Pinna, *Adv. Mater. Interfaces*, 2016, **3**, 1600335.
56 M. Z. Ansari, I. Hussain, D. Mohapatra, S. A. Ansari, R. Rahighi, D. K. Nandi, W. Song and S. H. Kim, *Adv. Sci.*, 2024, **11**, 2303055.
57 A. Rothman, S. Seo, J. Woodruff, H. Kim and S. F. Bent, *J. Vac. Sci. Technol., A*, 2024, **42**, 052402.
58 T. C. Ramli, C. J. Chen, H. H. Wang, C. Y. Tsao, I. C. Hsu, H. J. Ting and H. Y. Chen, *Macromol. Rapid Commun.*, 2025, 2401045.
59 B. Wei, F. Guo, F. Zhou, F. Fei, S. Zhang and F. Song, *J. Appl. Phys.*, 2025, **137**, 174301.
60 L. Liu, Y. Wang, F. Sun, Y. Dai, S. Wang, Y. Bai, L. Li, T. Li, T. Zhang and S. Qin, *Microsyst. Nanoeng.*, 2020, **6**, 31.
61 C. Zhang, T. Wang, G. Zhang, R. Gao, C. Gao, Z. Wang and F. Xuan, *Adv. Sci.*, 2025, **12**, e11555.
62 J. Li, Y. Li, N. Zhou, G. Wang, Q. Zhang, A. Du, Y. Zhang, J. Gao, Z. Kong and H. Lin, *Materials*, 2020, **13**, 771.
63 A. Lecestre, M. Martin, F. Cristiano, T. Baron and G. Larrieu, *ACS Omega*, 2022, **7**, 5836–5843.
64 L. J. Metzroth, E. M. Miller, A. G. Norman, S. Yazdi and G. M. Carroll, *Nano Lett.*, 2021, **21**, 9131–9137.
65 F. Hernandez-Ramirez, J. D. Prades, R. Jimenez-Diaz, T. Fischer, A. Romano-Rodriguez, S. Mathur and J. R. Morante, *Phys. Chem. Chem. Phys.*, 2009, **11**, 7105–7110.
66 C. Fàbrega, O. Casals, F. Hernandez-Ramirez and J. Prades, *Sens. Actuators, B*, 2018, **256**, 797–811.
67 H. Kang, S. Y. Cho, J. Ryu, J. Choi, H. Ahn, H. Joo and H. T. Jung, *Adv. Funct. Mater.*, 2020, **30**, 2002486.

68 T.-E. Song, C. W. Ahn and H.-J. Jeon, *Langmuir*, 2017, **33**, 8260–8266.
69 X. Chen, C. K. Wong, C. A. Yuan and G. Zhang, *Sens. Actuators, B*, 2013, **177**, 178–195.
70 M. Hjiri, F. M. Barakat and G. Neri, *Micro Nanostruct.*, 2025, 208299.
71 Z. Tang, F. Li, M. Peng, W. Fu, X. Liu, J. Zhang, G. Fei and M. Tu, *ACS Sens.*, 2025, **10**, 5520–5527.
72 L. Xu, Z. Dai, G. Duan, L. Guo, Y. Wang, H. Zhou, Y. Liu, W. Cai, Y. Wang and T. Li, *Sci. Rep.*, 2015, **5**, 10507.
73 K.-W. Choi, M.-H. Seo, J.-S. Lee, K. Kang, I. Park and J.-B. Yoon, Highly aligned suspended nanowire array for self-heating type gas sensors, 2017 IEEE 30th International Conference on Micro Electro Mechanical Systems (MEMS), 2017, pp. 191–194.
74 S.-H. Kim, M.-S. Jo, S.-Y. Park, K.-W. Choi, S.-H. Kim, J.-Y. Yoo, B.-J. Kim and J.-B. Yoon, *ACS Nano*, 2023, **17**, 23649–23658.
75 M.-S. Jo, B.-J. Kim, M.-K. Chung, S.-Y. Jung, M.-H. Seo, J.-Y. Yoo, J.-S. Yang, S.-H. Kim and J.-B. Yoon, *Nanoscale Adv.*, 2025, **7**, 1509–1517.
76 J. S. Lee, K. W. Choi, J. Y. Yoo, M. S. Jo and J. B. Yoon, *Small*, 2020, **16**, 1906845.
77 M.-S. Jo, K.-H. Kim, J.-S. Lee, S.-H. Kim, J.-Y. Yoo, K.-W. Choi, B.-J. Kim, D.-S. Kwon, I. Yoo and J.-S. Yang, *ACS Nano*, 2023, **17**, 23649–23658.
78 X. Tian, S.-M. Kim, J.-Y. Yoo, M.-S. Jo, J.-B. Yoon and M.-H. Seo, *ACS Appl. Mater. Interfaces*, 2025, **17**, 24513–24525.
79 J.-Y. Yoo, J.-S. Yang, M.-K. Chung, S.-H. Kim and J.-B. Yoon, *J. Micromech. Microeng.*, 2021, **31**, 074001.
80 K.-W. Choi, J.-S. Lee, M.-H. Seo, M.-S. Jo, J.-Y. Yoo, G. S. Sim and J.-B. Yoon, *Sens. Actuators, B*, 2019, **289**, 153–159.
81 J.-S. Lee, M.-H. Seo, K.-W. Choi, J.-Y. Yoo, M.-S. Jo and J.-B. Yoon, *Nanoscale*, 2019, **11**, 16317–16326.
82 M.-H. Seo, J.-Y. Yoo, S.-Y. Choi, J.-S. Lee, K.-W. Choi, C. K. Jeong, K. J. Lee and J.-B. Yoon, *ACS Nano*, 2017, **11**, 1520–1529.
83 M.-H. Seo, K. Kang, J.-Y. Yoo, J. Park, J.-S. Lee, I. Cho, B.-J. Kim, Y. Jeong, J.-Y. Lee and B. Kim, *ACS Nano*, 2020, **14**, 16813–16822.
84 A. Sharma, S. B. Eadi, H. Noothalapati, M. Otyepka, H. D. Lee and K. Jayaramulu, *Chem. Soc. Rev.*, 2024, **53**, 2530–2577.
85 S. Panda, S. Mehlawat, N. Dhariwal, A. Kumar and A. Sanger, *Mater. Sci. Eng., B*, 2024, **308**, 117616.
86 L. Liu, Y. Wang, F. Sun, Y. Dai, S. Wang, Y. Bai, L. Li, T. Li, T. Zhang and S. Qin, *Microsyst. Nanoeng.*, 2020, **6**, 31.
87 G. Liu, B. Wen, T. Xie, A. Castillo, J.-Y. Ha, N. Sullivan, R. Debnath, A. Davydov, M. Peckerar and A. Motayed, *Microelectron. Eng.*, 2015, **142**, 58–63.
88 L. Y. Zhu, K. P. Yuan, J. H. Yang, C. Z. Hang, H. P. Ma, X. M. Ji, A. Devi, H. L. Lu and D. W. Zhang, *Microsyst. Nanoeng.*, 2020, **6**, 30.
89 Z. Yuan, F. Yang, F. Meng, K. Zuo and J. Li, *IEEE Sens. J.*, 2021, **21**, 18368–18380.
90 M. Bonyani, S. M. Zebarjad, A. Mirzaei, T.-U. Kim, H. W. Kim and S. S. Kim, *J. Alloys Compd.*, 2024, **1001**, 175201.
91 N. Khomarloo, E. Mohsenzadeh, H. Gidik, R. Bagherzadeh and M. Latifi, *RSC Adv.*, 2024, **14**, 7806–7824.
92 W.-C. Huang, Y. Li, N.-H. Chang, W.-J. Hong, S.-Y. Wu, S.-Y. Liao, W.-J. Hsueh, C.-M. Wang and C.-Y. Huang, *Sens. Actuators, B*, 2024, **417**, 136175.
93 M. Deb, C.-J. Lu and H.-W. Zan, *ACS Sens.*, 2024, **9**, 4568–4577.
94 Z. Wu, Z. Chen, Z. Deng, N. Dai, Y. Sun and M. Ge, *RSC Adv.*, 2024, **14**, 12225–12234.
95 J. Liang, K. Wang, C. Xuan, Q. Chen, W. Tai, P. Ge and H. Zhang, *Sens. Actuators, A*, 2022, **347**, 113986.
96 L. Hao, J. Li, X. Wang, B. Yue, H. Shao, F. Li, T. Wang and X. Dong, *Sens. Actuators, B*, 2025, **433**, 137515.
97 M. S. Jo, S. H. Kim, S. Y. Park, K. W. Choi, S. H. Kim, J. Y. Yoo, B. J. Kim and J. B. Yoon, *ACS Sens.*, 2024, **9**, 1896–1905.
98 P. M. Bulemo, D. H. Kim, H. Shin, H. J. Cho, W. T. Koo, S. J. Choi, C. Park, J. Ahn, A. T. Guntner, R. M. Penner and I. D. Kim, *Chem. Rev.*, 2025, **125**, 4111–4183.
99 M. Seitz, J. Boisvere, B. Melanson, J. W. Morrell, N. H. Manimaran, K. Xu and J. Zhang, *iScience*, 2024, **27**, 109423.
100 R. K. Mondal, Y. J. Kim, Y. Liao, Z. Zheng, J. Dai and M. Kim, *J. Mater. Chem. C*, 2025, **13**, 3145–3166.
101 P. Ren, L. Qi, K. You and Q. Shi, *Nanomaterials*, 2022, **12**, 228.
102 Y. Park, H. Luan, K. Kwon, T. S. Chung, S. Oh, J.-Y. Yoo, G. Chung, J. Kim, S. Kim, S. S. Kwak, J. Choi, H.-P. Phan, S. Yoo, H. Jeong, J. Shin, S. M. Won, H.-J. Yoon, Y. H. Jung and J. A. Rogers, *npj Flexible Electron.*, 2024, **8**, 6.
103 A. Jannat, M. M. M. Talukder, Z. Li and J. Z. Ou, *Small Sci.*, 2025, **5**, 2500025.
104 G. Barandun, L. Gonzalez-Macia, H. S. Lee, C. Dincer and F. Guder, *ACS Sens.*, 2022, **7**, 2804–2822.
105 M. Kang, J.-K. Han, K. Lee, J. Jeong, C. Yoo, J. W. Jeon, B. Park, W. Choi, J. Ahn and K.-J. Yoon, *Sci. Adv.*, 2025, **11**, eadv9222.
106 J. Lee, M. Kim, S. Park, J. Ahn and I. D. Kim, *Adv. Mater.*, 2025, **37**, e08204.
107 I. Cho, Y. C. Sim, M. Cho, Y.-H. Cho and I. Park, *ACS Sens.*, 2020, **5**, 563–570.
108 M. Chowdhury and M. Oehlschlaeger, *ACS Sens.*, 2025, **10**, 1538–1563.
109 M. Harun-Or-Rashid, S. Mirzaei and N. Nasiri, *ACS Sens.*, 2025, **10**, 1620–1640.
110 R. Nivishna, P. Anilkumar and A. Nisha Jenifar, *Nano-Struct. Nano-Objects*, 2025, **44**, 101560.
111 I. Cho, K. Lee, Y. C. Sim, J.-S. Jeong, M. Cho, H. Jung, M. Kang, Y.-H. Cho, S. C. Ha and K.-J. Yoon, *Light: Sci. Appl.*, 2023, **12**, 95.

112 C. Han, X. Li, Y. Liu, Y. Tang, M. Liu, X. Li, C. Shao, J. Ma and Y. Liu, *Adv. Sci.*, 2021, **8**, 2102471.
113 S. Sonwal, K. S. Ranjith, S. Han, Y.-K. Han, M.-H. Oh and Y. S. Huh, *J. Mater. Chem. A*, 2024, **12**, 11004–11019.
114 S. Mandal, A. V. Marsh, H. Faber, T. Ghoshal, D. K. Goswami, L. Tsetseris, M. Heeney and T. D. Anthopoulos, *Nat. Electron.*, 2025, 1–10.
115 X. Zhao, B. Cai, Q. Tang, Y. Tong and Y. Liu, *Sensors*, 2014, **14**, 13999–14020.
116 G. Korotcenkov, *Mater. Sci. Eng., B*, 2007, **139**, 1–23.
117 E. Comini, G. Faglia, M. Ferroni, A. Ponzoni, A. Vomiero and G. Sberveglieri, *J. Mol. Catal. A: Chem.*, 2009, **305**, 170–177.
118 T. Zhai, L. Li, Y. Ma, M. Liao, X. Wang, X. Fang, J. Yao, Y. Bando and D. Golberg, *Chem. Soc. Rev.*, 2011, **40**, 2986–3004.
119 K. Lee, I. Cho, M. Kang, J. Jeong, M. Choi, K. Y. Woo, K.-J. Yoon, Y.-H. Cho and I. Park, *ACS Nano*, 2022, **17**, 539–551.
120 S. D. Lawaniya, S. Kumar, Y. Yu, H.-G. Rubahn, Y. K. Mishra and K. Awasthi, *Mater. Today Chem.*, 2023, **29**, 101428.
121 A. Jannat, M. M. M. Talukder, Z. Li and J. Z. Ou, *Small Sci.*, 2025, 2500025.
122 X. Zheng and H. Cheng, *Sci. China: Technol. Sci.*, 2019, **62**, 209–223.
123 F. Niu, F. Zhou, Z. Wang, L. Wei, J. Hu, L. Dong, Y. Ma, M. Wang, S. Jia and X. Chen, *Research*, 2023, **6**, 0100.
124 B. Wang, A. Thukral, Z. Xie, L. Liu, X. Zhang, W. Huang, X. Yu, C. Yu, T. J. Marks and A. Facchetti, *Nat. Commun.*, 2020, **11**, 2405.
125 M. Ma, X. Yang, X. Ying, C. Shi, Z. Jia and B. Jia, *Foods*, 2023, **12**, 3966.
126 K. Wu, M. Debliquy and C. Zhang, *Compr. Rev. Food Sci. Food Saf.*, 2023, **22**, 913–945.
127 S. J. Park, S. M. Lee, M.-H. Oh, Y. S. Huh and H. W. Jang, *Sustainable Food Technol.*, 2024, **2**, 266–280.
128 H. Jayan, R. Zhou, C. Sun, C. Wang, L. Yin, X. Zou and Z. Guo, *Foods*, 2025, **14**, 2706.
129 J. Yun, J.-H. Ahn, Y.-K. Choi and I. Park, Ultra-low power hydrogen sensor by suspended and palladium coated silicon nanowire, 2017 IEEE 30th International Conference on Micro Electro Mechanical Systems (MEMS), 2017, pp. 1079–1082.
130 H. Hashtroudi, P. Atkin, I. Mackinnon and M. Shafiei, *Int. J. Hydrogen Energy*, 2019, **44**, 26646–26664.
131 P. Yang, Y. Fan, K. Hu, L. Jiang, L. Tan, Z. Wang, A. Li, S. Yang, Y. Hu and H. Gu, *ACS Appl. Mater. Interfaces*, 2022, **14**, 25937–25948.
132 T. Hübert, L. Boon-Brett, G. Black and U. Banach, *Sens. Actuators, B*, 2011, **157**, 329–352.
133 R. Ramachandran and R. K. Menon, *Int. J. Hydrogen Energy*, 1998, **23**, 593–598.
134 S. Sharma and S. K. Ghoshal, *Renewable Sustainable Energy Rev.*, 2015, **43**, 1151–1158.
135 C. Wang, L. Yin, L. Zhang, D. Xiang and R. Gao, *Sensors*, 2010, **10**, 2088–2106.
136 I. Darmadi, F. A. A. Nugroho and C. Langhammer, *ACS Sens.*, 2020, **5**, 3306–3327.
137 Z. Li, A. A. Haidry, T. Wang and Z. J. Yao, *Appl. Phys. Lett.*, 2017, **111**, 032104.
138 S. Yang, Z. Wang, Y. Hu, X. Luo, J. Lei, D. Zhou, L. Fei, Y. Wang and H. Gu, *ACS Appl. Mater. Interfaces*, 2015, **7**, 9247–9253.
139 D. Zhang, L. Zhou, Y. Wu, C. Yang and H. Zhang, *Small*, 2024, **20**, 2406964.
140 C. Liewhiran, N. Tamaekong, A. Wisitsoraat and S. Phanichphant, *Sens. Actuators, B*, 2012, **163**, 51–60.
141 J. Yun, M. Cho, K. Lee, M. Kang and I. Park, *Sens. Actuators, B*, 2022, **372**, 132612.
142 J. Wei, Q. Peng, Y. Xie and Y. Chen, *Sensors*, 2025, **25**, 6321.
143 B. Zong, S. Wu, Y. Yang, Q. Li, T. Tao and S. Mao, *Nano-Micro Lett.*, 2025, **17**, 54.
144 C. Hu, W. Zhang, J. Yang, Y. Pei, X. Tan, B. Dong, H. Song and L. Xu, *Chem. Soc. Rev.*, 2025, **54**, 11302–11367.
145 Q. Hu, P. Solomon, L. Österlund and Z. Zhang, *Nat. Commun.*, 2024, **15**, 5259.